MODELING ELECTROSPINNING PROCESS
AND
A NUMERICAL SCHEME USING LATTICE BOLTZMANN METHOD TO SIMULATE VISCOELASTIC FLUID FLOWS

A Thesis

by

SATISH KARRA

Submitted to the Office of Graduate Studies of
Texas A&M University
in partial fulfillment of the requirements for the degree of

MASTER OF SCIENCE

May 2007

Major Subject: Mechanical Engineering

MODELING ELECTROSPINNING PROCESS

AND

A NUMERICAL SCHEME USING LATTICE BOLTZMANN METHOD TO SIMULATE VISCOELASTIC FLUID FLOWS

A Thesis

by

SATISH KARRA

Submitted to the Office of Graduate Studies of
Texas A&M University
in partial fulfillment of the requirements for the degree of

MASTER OF SCIENCE

Approved by:

Co-Chairs of Committee,	Arun R. Srinivasa
	Sharath Girimaji
Committee Member,	N.K. Anand
Head of Department,	Dennis O'Neal

May 2007

Major Subject: Mechanical Engineering

ABSTRACT

Modeling Electrospinning Process

and

A Numerical Scheme using Lattice Boltzmann Method to Simulate Viscoelastic Fluid Flows. (May 2007)

Satish Karra, B.Tech, Indian Institute of Technology Madras, Chennai, India

Co–Chairs of Advisory Committee: Dr. Arun R. Srinivasa
Dr. Sharath Girimaji

In the recent years, researchers have discovered a multitude of applications using nanofibers in fields like composites, biotechnology, environmental engineering, defense, optics and electronics. This increase in nanofiber applications needs a higher rate of nanofiber production. Electrospinning has proven to be the best nanofiber manufacturing process because of simplicity and material compatibility. Study of effects of various electrospinning parameters is important to improve the rate of nanofiber processing. In addition, several applications demand well-oriented nanofibers. Researchers have experimentally tried to control the nanofibers using secondary external electric field. In the first study, the electrospinning process is modeled and the bending instability of a viscoelastic jet is simulated. For this, the existing discrete bead model is modified and the results are compared, qualitatively, with previous works in literature. In this study, an attempt is also made to simulate the effect of secondary electric field on electrospinning process and whipping instability. It is observed that the external secondary field unwinds the jet spirals, reduces the whipping instability and increases the tension in the fiber.

Lattice Boltzmann method (LBM) has gained popularity in the past decade as the method is easy implement and can also be parallelized. In the second part of this thesis, a hybrid numerical scheme which couples lattice Boltzmann method with finite difference method for a Oldroyd-B viscoelastic solution is proposed. In this scheme, the polymer viscoelastic stress tensor is included in the equilibrium distribution function and the distribution function is updated using SRT-LBE model. Then, the local velocities from the distribution function are evaluated. These local velocities are used to evaluate local velocity gradients using a central difference method in space. Next, a forward difference scheme in time is used on the Maxwell Upper Convected model and the viscoelastic stress tensor is updated. Finally, using the proposed numerical method start-up Couette flow problem for $Re = 0.5$ and $We = 1.1$, is simulated. The velocity and stress results from these simulations agree very well with the analytical solutions.

ACKNOWLEDGMENTS

I would like to thank Dr. Arun Srinivasa for his support and motivation throughout this work and for his guidance on vital decisions related to my career. I would also like to sincerely thank Dr. Girimaji for giving me an opportunity to work with him and helping me financially.

I would also like to thank my parents who have been there for me through good and bad times. Finally, I would like to thank my friends and colleagues: Vijay Idimadakala, Hari, Swaroop, Chaitanya, Anshul, Vijay Sathyamurthi, Nandagopalan and Praveen.

TABLE OF CONTENTS

LIST OF FIGURES

FIGURE Page

FIGURE Page

CHAPTER I

INTRODUCTION

Substances like polymers, emulsions, colloids which show both solid-like and fluid-like behavior are viscoelastic in nature. However, when an external stress is applied, a viscoelastic fluid's transient response is much larger than the time scales of the instrument used [1]. In a viscoelastic fluid, the stress tensor depends on the history of the deformation gradient [2]. Due to their vast applications, viscoelastic fluids have been studied for several decades to understand the phenomena associated with it. For instance, polymers are widely used in applications like automobiles, textile industry and composites. In these applications, the polymer is usually used in a fluid form, either as a melt or either dissolved in a solvent. These polymers are shaped commonly by spinning process or through extrusion process. The problem of spinning has been studied for several decades and some of theoretical works in this area have been done by Kannan and Rajagopal [3] and Bechtel [4]. In the extrusion of viscoelastic fluids several interesting and complex phenomena, some of them due to instability, have been observed. These phenomena include extrude die swell, sharkskin effect, spurting. Several theoretical and experimental, have been done to explain and model these phenomena [5, 1].

Another viscoelastic flow problem which has been studied in the recent years is the electrospinning jet formation problem. Polymer nanofiber research has gained momentum in the last decade due to the vast applications of nanofibers [6]. Electrospinning, which was initially developed by Formhals (See [6] for reference) in 1934, was re-discovered a decade ago, as a powerful process to produce nanofibers. Electrospin-

---

The journal model is *IEEE Transactions on Automatic Control*.

ning has been found to have several advantages over classical spinning processes and other nanofiber manufacturing processes. Unlike, classical spinning process which mainly uses gravity and externally applied tension, electrospinning uses externally applied electric field, as driving force. In electrospinning, instabilities like Taylor instability and whipping instability were also observed; though the reason behind these instabilities is still not clear. Further, in electrospinning nanofibers form a random mesh and certain nanofiber applications demand highly oriented nanofibers. Research is being done to control the nanofiber orientation using a secondary external field [7]. Modeling and simulation of electrospinning process will help us understand the following:

- the cause for whipping instability.
- the dependence of jet formation and jet instability on the process parameters and fluid properties, for better jet control and higher production rate.
- the effect of secondary external field on jet instability and fiber orientation.

With this motivation, we attempt to model and simulate the jet formation in electrospinning, in the first part of this thesis.

Also, several works have been done to solve and understand viscoelastic flow problems like die-swelling extrusion problem and jet buckling problem using traditional numerical techniques like finite volume [8], finite difference [9] and finite element [10]. These techniques, in general, have been found to be less effective and more computationally intensive compared to a more recently developed lattice Boltzmann method [11, 12]. LBM involves simple arithmetic and so this method easy to implement. Further, LBM can be can parallelized as the computations are local. Hence, LBM can be used for large-scale computations [13] and problems involving complex fluids [13],

colloidal suspensions [14] and moving boundaries [15] can been easily solved using LBM. Due to these advantages of LBM over traditional CFD schemes, a LBM based technique which models viscoelastic fluid behavior is valuable. However, very few works have been done in this aspect [16, 17]. Hence, in the second part of this thesis, we explore the use of LBM to viscoelastic fluid flows.

The objectives of the thesis can be summarized as follows:

- Model and simulate electrospinning jet flow and whipping instability.
- Develop a hybrid numerical using the lattice Boltzmann method to solve the viscoelastic flow problems.

The outline of the thesis is as follows: In chapter II, we first discuss the background of electrospinning and review the previous works on elecstrospinning modeling and simulation. Then, we discuss our model and simulations for the electrospinning process along with the basic assumptions. In chapter III, we first review previous works that used lattice Boltzmann method. We also present the continuum governing equations for viscoelastic fluid flows. We then develop our hybrid numerical scheme using LBM and finite difference method for Oldroyd-B polymer solutions. We then simulate start-up Couette flow with our scheme and compare the results with the analytical solution. Finally, we summarize the thesis in chapter IV.

CHAPTER II

MODELING ELECTROSPINNING PROCESS

A. Introduction

In the recent years, nanoscale research has grown tremendously in the fields of science and engineering, all over the world. Some of the fields include biology and medicine (nanobioengineering), material science (nanoprocessing and nanomaterials), electronics and chemistry. Huang et al. [18] have done extensive study on the growth in nanoscience and engineering patents - field, country and institution wise. Ramakrishna et al. [19] said that if the characteristic dimensions of the research are less than 100 nm, then the research can be considered as a part of nanotechnology. In general, a fiber can be defined as a slender, thread like object, and Ramakrishna et al. [19] defined a nanofiber as a nanomaterial with respect to diameter. Hence, one can define a nanofiber as a slender, thread like object, with diameter less than 100nm.

Nanofibers, due to large surface to volume ratio and better mechanical properties compared to microfibers [6], have multitude of applications. Some of the applications include tissue engineering, composite engineering, defense and environmental engineering. In medicine and biology, nanofibers are used to make tissue scaffolds. Nanofibers have also proven to improve the mechanical characteristics of composites. Biological and chemical filters which have numerous applications in defense and environmental engineering are being developed using nanofibers [6, 19].

In section B, we discuss the manufacturing processes used to develop nanofibers followed by the applications of nanofibers in section C . Then, in section D we discuss the electrospinning process in detail, followed by a review on electrospinning jet instabilities in section E. We discuss the importance of electrospinning in section E.

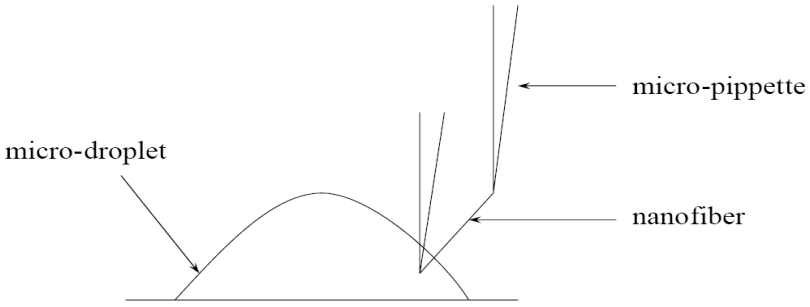

Fig. 1. Schematic of drawing process [19]. Each fiber is drawn from a micro-droplet of polymer solution using a micropipette.

In section F, we review the literature on modeling and simulations of electrospinning. We then present our model with simulations and compare the results with previous works in literature [20, 21] in sections I and J. We also discuss the effects of applied secondary external field on jet instability based on our simulations. Finally, we conclude the chapter with a summary and recommendations for future work in section K.

B. Nanofiber processing

The basic manufacturing processes used for making nanofibers are:

Drawing: Fibers with diameter of the order 1mm can be produced using the usual drawing process. However, to get a nanofiber, each fiber is pulled from a microdroplet (see Fig.1). The drawing is accompanied by evaporation of the solvent, leading to solidification of the fiber. In this method, the length of the nanofiber drawn is of the order of microns and only one fiber can be made at a time [22].

Template synthesis: This process is similar to the extrusion process in manufac-

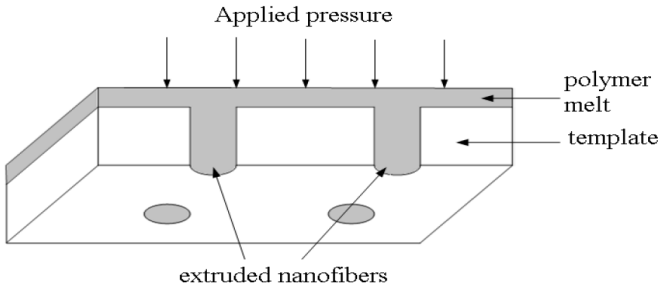

Fig. 2. Schematic of template synthesis [23]. Pressure is applied on the polymer and the polymer extrudes through a nanoporous template.

turing. Nanoporous filtration membrane is used as a template (see Fig.2). Nanofibers are produced when the polymer is extruded through these nanopores under pressure. Martin [23] has produced nanotubules of various metals, carbons and semiconductor materials using this process.

Gelation: Initially, a gel is made using pre-determined amounts of polymer and solvent followed by phase separation and gel formation. Finally, nanofiber matrix forms when the gel is frozen and freeze-dried [24, 25]. Notice that in this method a matrix forms in this process instead of a single fiber.

Self-assembly: In nano-manufacturing, a material of desired dimensions can be processed either using top-down or bottom-up technique [19, 25]. In the top-down method, a larger size of the material is cut till the desired size is achieved. On the other hand, in the bottom-up method, the desired size is achieved by building from molecules. Self-assembly is a bottom-up technique and in self-assembly, stable and ordered structures are formed from disordered entities of molecules. Typically, non-covalent bonds like hydrogen bonds and electrostatic forces are responsible for self-assembly [25]. See [26] for detailed description of self-assembly and applications

along with a formal definition. In self-assembly of nanofibers, the smaller disordered parts of nanofiber combine to form a much ordered nanofiber. Hartgerink et al. [27] discussed in detail about the formation of peptide nanofibers with self-assembly.

C. Applications of nanofibers

Nanofibers have high surface to volume ratio (order of 1000). Most of the applications of nanofibers like drug delivery, filtration, cosmetics and protective clothing are based on this characteristic. Other applications like nanocomposites explore the better mechanical characteristics of nanofibers compared to microfibers [6].

Naturally found materials like silk, collagen, polysaccharide cellulose and keratin are in fiber form. Hence, nanofiber technology can be used to mimic these biological materials and research in this aspect of nanofibers is vital [25] . Research has been done to use biodegradable nanofibers as scaffolds to tissues. These tissues include bones, cartilages and blood vessels [25]. These nanofibers act as tissue template over which the human cells can grow.

Polymer nanofibers can be used as carriers for drug delivery. It has been found that the drug material dissolution rate highly depends of the surface area of the carrier as well as the drug. Nanofibers have an advantage in this aspect due to their large surface area to volume ratio [6].

Further, nanofibers of certain biologically active polymers can be used as wound dressing. Wound dressings typically should prevent bacteria and dust and should allow air transfer. Several works have been published (see [25] for references) which have tested nanofiber usage for wound dressings. Moreover, patents have been filed and several works have been published, which use nanofiber technology to make medical prostheses. Also, due to their superior mechanical properties, nanofiber composites

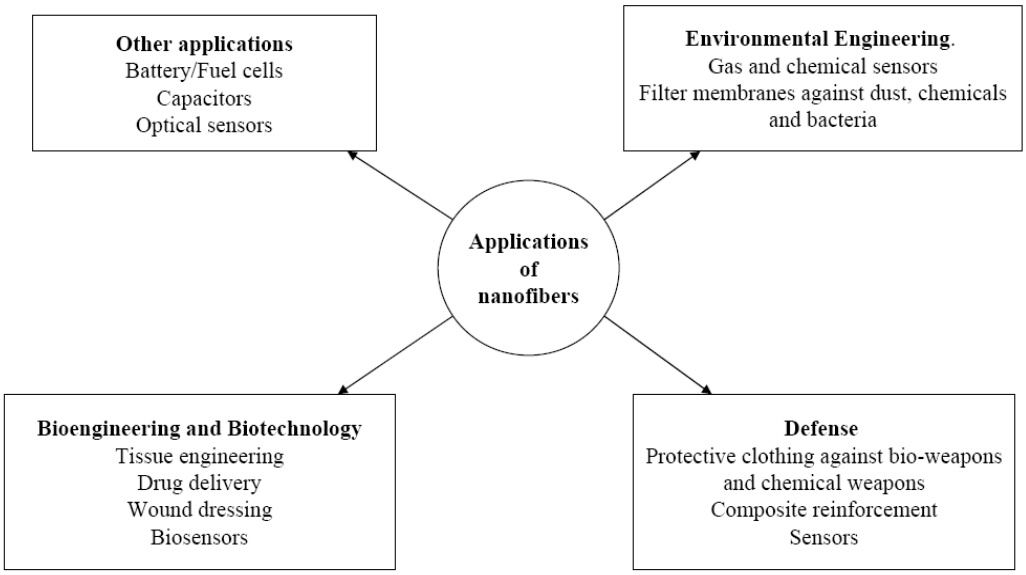

Fig. 3. Schematic showing the application of nanofibers in the fields of biotechnology and biomedical, environmental engineering, defense and other applications like optics [6, 19].

are used in fillers for dental purposes.

Due to high surface area to volume ratio, nanofibers can be used for molecular separation and filtration. Further, nanofiber meshes can be used as skin care masks as they block dust particles. In addition, the higher surface area allows quicker transfer rate of the mask additives. Nanofiber meshes can act as protective clothing from biological as well as chemical agents because of their excellent potential for filtration. Finally, nanofibers can be used to make bio-sensors, and to preserve and store biologically active substances like enzymes (see Zhang et al. [25] for references with regard to biotechnology and biomedical applications).

As the electric conductivity highly depends on the surface area, nanofibrous membranes made from a conductive material can be used as electrode for batteries [6]. Nanofibrous membranes can also be used as highly responsive fluorescence optical sensors [28]. Also, nanofibers from electrospinning can be used to make templates in template synthesis to develop nanotubes that cannot be processed using electrospinning [29]. Fig.3 shows an overview of various applications of nanofibers.

D. Electrospinning

Typically, a polymer solution or polymer melt is placed in a syringe with outlet diameter of the order of 1mm and a hemispherical droplet forms at the outlet. A copper plate placed at a distance of around 20 cm from the syringe acts as a collector. A high voltage power supply with a range of 15 KV to 20 KV is applied to maintain potential difference between the droplet and the copper plate. For this, a lead wire from high voltage supply is placed into the polymer solution/melt and the copper plate is grounded. This potential difference creates an electric field external to the polymer solution/melt. The schematic of the basic set-up is shown in Fig.4.

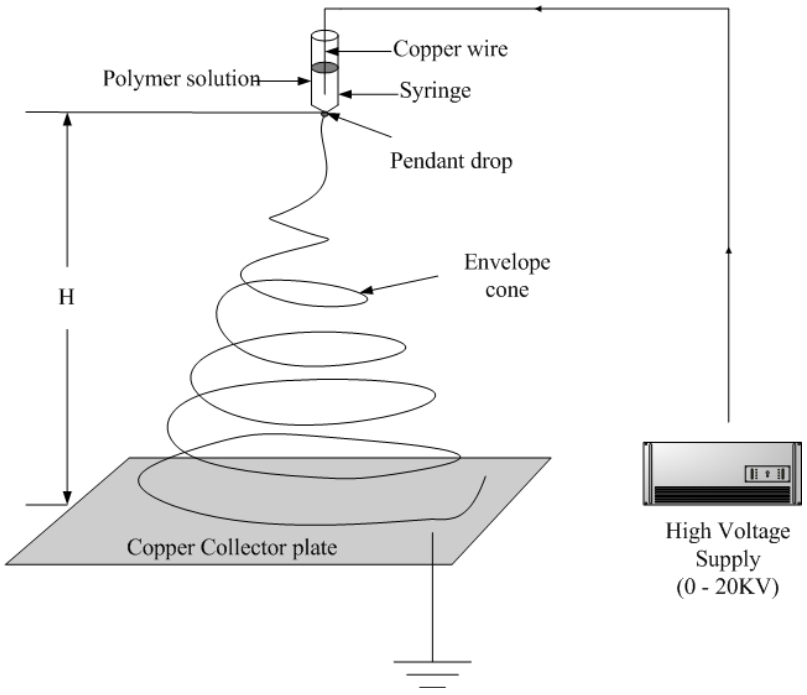

Fig. 4. Schematic of basic electrospinning set-up with the whipping instability of jet. Typically a potential difference of 15 – 20 KV is applied across the syringe with polymer solution and the copper collector. Here, H is the distance between the syringe and collector (which is typically of the order of 15 – 20 cm). The secondary instabilities [20] are not shown.

Initially, the polymer solution is uncharged in the absence of external electric field. During this uncharged state, the number of positive and negative ions in the solution is the same. Hence, there is no electric field within the solution also. Now, when the power is switched on, negative ions in the solution migrate to anode (positive electrode) while the positive ions migrate to the cathode (negative electrode). The migration of ions causes an excess charge per unit volume of the solution and creates an electric field in the solution/melt. By adding a soluble salt, the conductivity of the polymer solution can be increased. However, the excess charge does not increase, since a salt gives equal number of positive and negative ions [20].

Now, as the potential difference is increased, the hemispherical droplet elongates to form a prolate and finally tends to a conical shape known as the Taylor cone [30, 31]. At a particular threshold potential difference, when the forces due to the electric field and the electrostatic repulsion overcome the surface tension forces, jet initiates. The jet remains axisymmetric for some distance. Then an instability called bending or whipping instability starts. This instability makes the jet to loop in spirals with increasing radius. The envelope of this loop or curve is a cone. Further, the electric field accelerates the jet and so the jet velocity increases. This leads to a decrease in the jet diameter (diameter decreases to an order of 10-100 nm), by mass conservation. In addition, the electrostatic repulsion between due to excess charges in the solution stretches the jet. This stretching also decreases the jet diameter.

The polymer solution content in the syringe or capillary decreases in the process and is usually supplied continuously through a syringe pump. The volumetric flow of the polymer solution varies from 1μl/min to 1ml/min. Further, the solvent evaporates and the jet solidifies as it reaches the collector plate. Finally, a mesh of randomly oriented solid nanofibers forms on the collector plate.

E. Instabilities in jet formation observed in electrospinning

Initially, a pendant droplet of the polymer solution/melt forms at the end of the syringe. When the force due to potential difference exceeds the force due to surface tension, a jet initiates. Taylor [30] studied the jet formation from the electrically charged pendant droplet. Taylor showed that a charged droplet destabilizes when the force due to its own electric field exceeds the surface tension force. He also showed, theoretically, that as the potential on the droplet surface is increased to its critical value (i.e., at the potential which initiates instability) the shape of the

droplet becomes less prolate and more spherical. However, Yarin et al. [31] showed experimentally that, in reality, the shape becomes more and more prolate as the potential is increased to threshold potential. Further, Taylor in his work, showed that at a particular threshold potential the droplet destabilizes into a conical jet with an angle of 49.3^o called the Taylor cone. Yarin et al. [31] showed that the Taylor cone solution corresponds to a particular self-similar solution while there exist cone shapes for other non self-similar solutions. They found that the cone angle where stability is lost, is 33.5^o and not 49.3^o.

Doshi and Reneker [32] interpreted that the diameter continuously decreases due to stretching of the jet and due to continuous evaporation. Also, they said that the increased charge density split the jet into further smaller jets. This phenomenon is called jet splaying. However, Shin et al. [33] showed from experiments that the rapid whipping of a single larger jet appeared like the formation of several smaller jets. Reneker [20] in their experiments observed secondary and tertiary instabilities.

Jaworek and Krupa [34] discussed the formation of different modes in electrohydrodynamic spraying of liquids. They performed experiments to study the effect of applied voltage on droplet and jet formation outside a capillary for viscous fluids. They used a set-up similar to electrospinning but their fluid was distilled water. Distilled water at a constant flow rate $40mm^3$ was supplied using a syringe pump to a stainless-steel capillary. This capillary was place $300mm$ above a collector plate and potential difference was applied between the capillary and the collector plate. Initially, from zero to 10 KV potential difference, droplets of distilled water were observed to drip from the capillary as force of gravity and electric forces overcome the surface tension force. This mode was called the dripping mode. At around 9KV, a small droplet smaller than capillary diameter was observed to form which detached from the capillary. This mode is called the micro-dripping mode. At higher voltages,

11-20 KV, the liquid elongated in the direction of the electric field and jets formed. However, the high electric field detached these jets and the detached jets split into several smaller droplets. This mode was called the spindle mode. When the potential difference was in the range 20-25 KV, these jets oscillated. Further increase of the voltage to around 30 KV lead to axisymmetric conical jets. In these jets two types of instabilities were observed: varicose and kink. In varicose instability the axis of the jet remained the same but waves were generated on the surface of the jet. While in kink instability, the axis of the jet moved irregularly away from the axis of the capillary. Further in the second type of instability, the jet was observed to split into several droplets. This mode was called as conical jet mode. This final mode is also observed in the electrospinning process.

Hohman et al. [35, 36] in their papers identified mainly two types of instability in an electrospinning jet: Rayleigh instability and whipping instability. Note that this Rayleigh instability in electrospinning is equivalent to the varicose instability in the experiments performed by Jaworek and Krupa. While the whipping instability mentioned by Hohman et al. is similar to the kink instability seen by Jaworek and Krupa.

Hohman et al. in their first paper [35] developed a stability analysis for the axisymmetric Rayleigh instability as well as the non-axisymmetric whipping instability in Newtonian fluids. According to them, the Rayleigh instability due to electrical forces is equivalent to the surface tension based Rayleigh instability. Further, they observed that in the absence of the surface charges, the Rayleigh instability dominated while increase in field and surface charge density improved the whipping instability. In addition, it was found that the whipping conducting instability strongly depended on the jet fluid parameters like conductivity, viscosity and dielectric constant.

F. Importance of electrospinning

Comparison of electrospinning with classical fiber spinning

In classical spinning (melt-spinning or dry spinning) process, the jet diameter highly depends on the orifice diameter. Typically, the diameter of the orifice is of the order of 0.1 mm. To reduce the diameter of the fiber, the jet is stretched due to constant tension from the roller. The other end of the jet solidifies as it rolls. Other forces acting on the jet are the forces due to surface tension and gravity. Now, in order to get a final diameter of the order or nanometer, one method is to increase the distance between the jet orifice and the roller. But to get such high draw ratio, the distance between the orifice and the roller should be of the order of several kilometers. Such high distances will: (a) increase the cost of production, (b) cause jet break-up due to Rayleigh instability. The other way to get a nanometer order diameter is to increase the tension to large values. Such high tension can lead to mechanical fracture of the fiber jet [21]. On the other hand, in electrospinning the distance between the source and collector is only of the order of 20cm and at such small distance we get nanofibers. In electrospinning, the causes for jet diameter decrease are: (a) the stretching due to the electro-static repulsion between the charges in the polymer solution, (b) the acceleration of the jet. Hence, electrospinning is a much better process than classical fiber spinning to make fibers with nanometer diameters.

Comparison of electrospinning with other nanofiber processing methods

In section B, we discussed the various polymer nanofiber manufacturing methods. Drawing, as mentioned, is not a continuous process and only one fiber is drawn at a time. Similarly, gelation and self-assembly are laboratory based processes and rate of nanofiber production is very slow. In template synthesis, though we can get more

than one nanofiber at a time, the process is not continuous and nanofibers that are only several microns in length are produced. On the other hand, electrospinning is continuous process and nanofibers upto several meters in length can be produced without breaking. Hence, electrospinning has tremendous advantage over other nanofiber processing techniques.

Other advantages of electrospinning process are:(a) simplicity: electrospinning is easy to set up, (b) material compatibility: about 50 polymers have shown to be compatible with electrsopinning [19, 6]. Huang et al.[6] provide a list of: polymers that have been used, various solvents for each polymer and the concentrations of the polymer in the solvent. The applications of the polymer nanofibers along with their possible uses have also been shown in the same paper. Also, a list of polymers that have been used in melt form rather than in a solution form, is given in the paper.

Due to above mentioned advantages of electrospinning process, researchers in the nanofiber field have identified the importance and potential of electrospinning for nanofiber production. Currently, development of better electrospinning techniques is a major part of nanofiber research [6, 37]. Nanofiber material characterization and nanofiber applications are the other major areas of nanofiber research.

G. Modeling and simulation of electrospinning

Although electrospinning gives continuous fibers, with the current knowledge electrospinning cannot be used for mass production [6]. Theron et al. [38] used multiple jets to improve the production rate. The other issue of current importance is controlling the nanofibers. In electrospinning, the nanofibers form a random mesh on the collector plate. However, some of the applications of nanofibers in device fabrication like microelectronics [39] and tissue engineering [7] need well-oriented nanofibers.

Researchers have controlled the nanofibers orientation by using dynamic mechanical collector devices like grounded rotating drums [7]. The other method to control the nanofibers is to manipulate the external field (usually by applying a secondary field) [7]. Modeling and simulations will give a better understanding of electrospinning jet mechanics. Also, the effect of secondary external field can be studied using simulation studies.

Till date two major modeling zones have been identified [40]. These zones are: (a) the zone close to the capillary outlet where an axisymmetric jet exits and thins down , (b) the whipping instability zone where the jet spirals and accelerates towards the collector plate.

For the jet initiation zone, Taylor had initially proposed the theory of formation of Taylor cone [30] which was later rectified by Yarin et al [31]. Hohman et al.[35] did theoretical work on the variation of the jet radius and have compared their results with experiments. Feng [41] proposed a model based on slender-body theory and compared the results for jet initiation zone with results obtained by Hohman and others [35]. Feng, in his later work [40] studied the jet thinning phenomenon using slender body approximation for a Giesekus fluid.

Reneker et al. [20] were the first to propose discrete bead model to model the whipping instability zone. They compared their results with experiment on polyethylene oxide dissolved in ethanol/water mixture. Solidifcation of the polymer was not considered in this model. Due to this, the result from their simulations were far from reality. Hohman et al. [35] also studied the behavior of jets in the whipping instability region. Later, Yarin et al. [42] modified their earlier proposed discrete bead model and considered solidification effect of the polymer. Results from this new model matched well with experiments. Recently, Kowalewski et al. [21] modified the surface tension and Coulombic interaction terms in discrete bead model. They stud-

ied the effects of various parameters like viscosity, elasticity and surface tension on jet stability, in their Jaworeck and Krupa also performed rigorous theoretical study and modeled the various modes of electrohydrodynamics.

Huang et al. [6] mentioned techniques using molecular dynamics modeling single nanofiber. According to them, Monte Carlo method, which stochastically determines properties, can be used to model single nanofibers. The other method uses deterministic molecular dynamics in which the configuration of the nanofiber molecules is determined using Newton's laws.

H. Objectives of this study

As discussed in section G, modeling and simulation of electrospinning jet will give us better understanding of the process. Hence, in this part of the work, we model and simulate the electrospinning jet and the whipping instability. Also, as discussed, control and organization of nanofibers is crucial. Although there are experimental works in literature which analyze the effect of secondary external field [7], there are no simulation works. In this work, we use our simulations to study the effect of field manipulation on jet whipping instability. The specific objectives of this part of the thesis are as follows:

1. We propose modifications in the discrete bead model existing in literature and make a qualitative comparison of our results with the simulations studies done by Reneker et al. [20] and Kowalewski et al. [21]. We change the surface tension interaction term in the momentum balance equation of the discrete bead model (see [20, Equation 20]). We use the surface tension force expression that was used by Kowalewski et al. [21]. We do not consider effect of polymer solidification in our model.

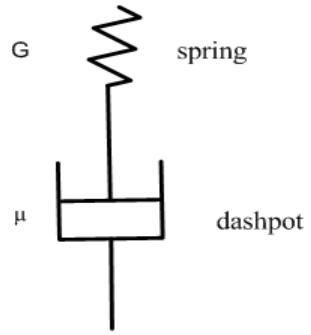

Fig. 5. Schematic showing Maxwell's spring (which models the elastic part with Young's modulus G) and dashpot (which models viscous part with viscosity μ) model for viscoelasticity.

2. We also investigate the effects of application of secondary electric field to the electrospinning process.

I. Discrete bead model: method and governing equations

The discrete bead model was initially proposed by Reneker et al. [20] In this model and in our work, the assumptions are as follows:

- The fluid jet is assumed to be a slender-body where the radial effects are negligible.
- The jet is split into several equal segments and the ends of each segment is modeled as a viscoelastic dumbbell or a bead similar to Maxwell's dumbbell (see Fig.5).

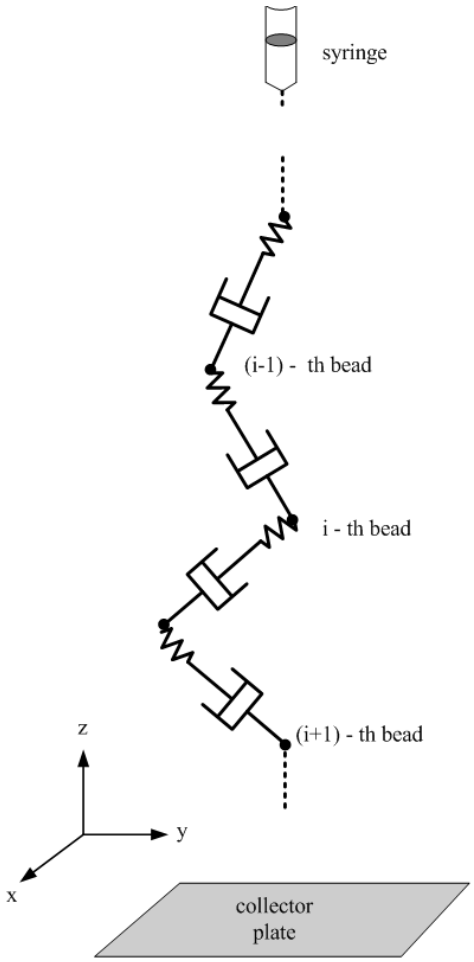

Fig. 6. Schematic showing the discrete bead model where the fluid jet is split into several beads. The figure also shows Maxwell's spring and dashpot model for viscoelasticity between the beads.

- The dumbbells are assumed to be of the same charge, which models the excess charge a unit volume of the jet. The charge on each dumbbell leads to a Coulombic interaction between the dumbbells in the system. Also, there is no electrical conductivity along the jet i.e., the jet is a perfect insulator.
- The background electric field caused due to potential difference is axial and uniform (capacitor field).
- The properties are constant.
- The effects of gravity and air drag are negligible (see [20]).
- The jet initiation zone is not considered for simulations.
- The beads are of the same mass and same charge.
- Solidification of the polymer is not considered.

Fig.6 shows the three dimensional discrete bead model for the entire jet. The figure also shows the $(i-1)$-th, i-th and the $(i+1)$-th beads with a spring and a dashpot between the beads. The spring and dashpot between the beads models the viscoelasticity of the polymer fluid. This was initially proposed by Maxwell [5].

Based on above mentioned assumptions, the governing equations for the entire system are as follows: By continuity we must have,

$$\pi a^2 l = \pi a_0^2 L \tag{2.1}$$

where a_0, L are the initial fiber radius and fiber segment length respectively, a, l are the fiber radius and fiber segment length at any instant.

Using Maxwell's law for linear viscoelasticity (Spring and dashpot model – Fig.5), the viscoelastic interaction between the fiber segment given by i-th and (i-1)-th beads

can be given as

$$\frac{1}{G}\frac{d\sigma_{ui}}{dt} = \frac{1}{l_{ui}}\frac{dl_{ui}}{dt} - \frac{1}{\mu}\sigma_{ui} \tag{2.2}$$

while the viscoelastic interaction between the i-th and the (i+1)-th beads in given by

$$\frac{1}{G}\frac{d\sigma_{di}}{dt} = \frac{1}{l_{di}}\frac{dl_{di}}{dt} - \frac{1}{\mu}\sigma_{di} \tag{2.3}$$

with $l_{ui} = |\mathbf{r}_i - \mathbf{r}_{i-1}|$, $l_{ui} = |\mathbf{r}_{i+1} - \mathbf{r}_{i-1}|$ where $\mathbf{r}_i$, $\mathbf{r}_i$, $\mathbf{r}_{i+1}$ are the position vectors of $(i-1)$-th, i-th, $(i+1)$-th beads with respect to the syringe outlet. G is the Young's modulus and μ is the dynamic viscosity of the fluid.

The Coulombic interaction between the i-th bead and the rest of the beads in the system is given by

$$\mathbf{F}_{Coulombic} = \sum_{j=1, j\neq i}^{N} \frac{e^2}{R_{ij}^3}(\mathbf{r}_i - \mathbf{r}_j) \tag{2.4}$$

where R_{ij} is the distance between i-th and j-th bead,e is the charge on each bead, N is the total number of beads in the system.

The force due to the external electric field is given by $e\frac{V_0}{H}$ with the direction pointing towards the collector plate and away from the syringe.

The force due to surface tension on the i-th bead due the adjacent segments can be written as [21]

$$\mathbf{F}_{surface\ tension} = \pi a_{di}\alpha\frac{\mathbf{r}_{i+1} - \mathbf{r}_i}{|\mathbf{r}_{i+1} - \mathbf{r}_i|} - \pi a_{ui}\alpha\frac{\mathbf{r}_i - \mathbf{r}_{i-1}}{|\mathbf{r}_i - \mathbf{r}_{i-1}|} \tag{2.5}$$

where α is the surface tension. Notice that the surface tension force term is different from the force used in [20]. Reneker et al. evaluated the surface tension based on the average diameter for the segment joining $(i-1)$-th, i-th beads and the segment joining $(i+1)$-th, i-th beads. Further, jet curvature was calculated using the $(i-1)$-th, i-th

and $(i+1)$-th bead co-ordinates.

Co-ordinate system: The xy-plane is parallel to the collector plate and z-axis points towards the syringe away from the collector plate. The projection of the syringe on the collector plate is the origin. Finally, using above force interactions the momentum conservation for i-th bead is

$$\begin{aligned} m\frac{d^2\mathbf{r}_i}{dt} = &\sum_{j=1,j\neq i}^{N} \frac{e^2}{R_{ij}^3}(\mathbf{r}_i - \mathbf{r}_j) - e\frac{V_0}{H}\mathbf{k} + \frac{\pi a_{ui}^2 \sigma_{ui}}{l_{ui}}(\mathbf{r}_{i+1} - \mathbf{r}_i) \\ &- \frac{\pi a_{di}^2 \sigma_{di}}{l_{di}}(\mathbf{r}_i - \mathbf{r}_{i-1}) + \pi a_{di}\alpha\frac{\mathbf{r}_{i+1} - \mathbf{r}_i}{|\mathbf{r}_{i+1} - \mathbf{r}_i|} - \pi a_{ui}\alpha\frac{\mathbf{r}_i - \mathbf{r}_{i-1}}{|\mathbf{r}_i - \mathbf{r}_{i-1}|} \end{aligned} \tag{2.6}$$

where m is the mass of the bead, $\mathbf{k}$ is the unit vector in the z-direction.

In this model, $i = 1$ is the bottom-most bead or the bead closest to the collector and $i = N$ is the top-most bead or the bead closest to the syringe. We non-dimensionalize equation (2.6) with the scheme used by Reneker et al [20] and solve the set of ordinary differential equations in (2.2), (2.3) and (2.6) using MATLAB. Also, we add a small initial perturbation (0.001) to the x and y positions of the bead coming out of the syringe, in our simulations. This perturbation is given to initialize the whipping instability due to the electrical forces. In addition, a when a bead traverses a distance of $H/2000$, we add a new bead to the system. This way the distance between a bead and its adjacent bead is always the same or in other words, all the segments have the same length. Further, we assume that the bead coming from syringe travels at a constant velocity in the negative z direction i.e., towards the collector plate, for sometime (similar to [21]).

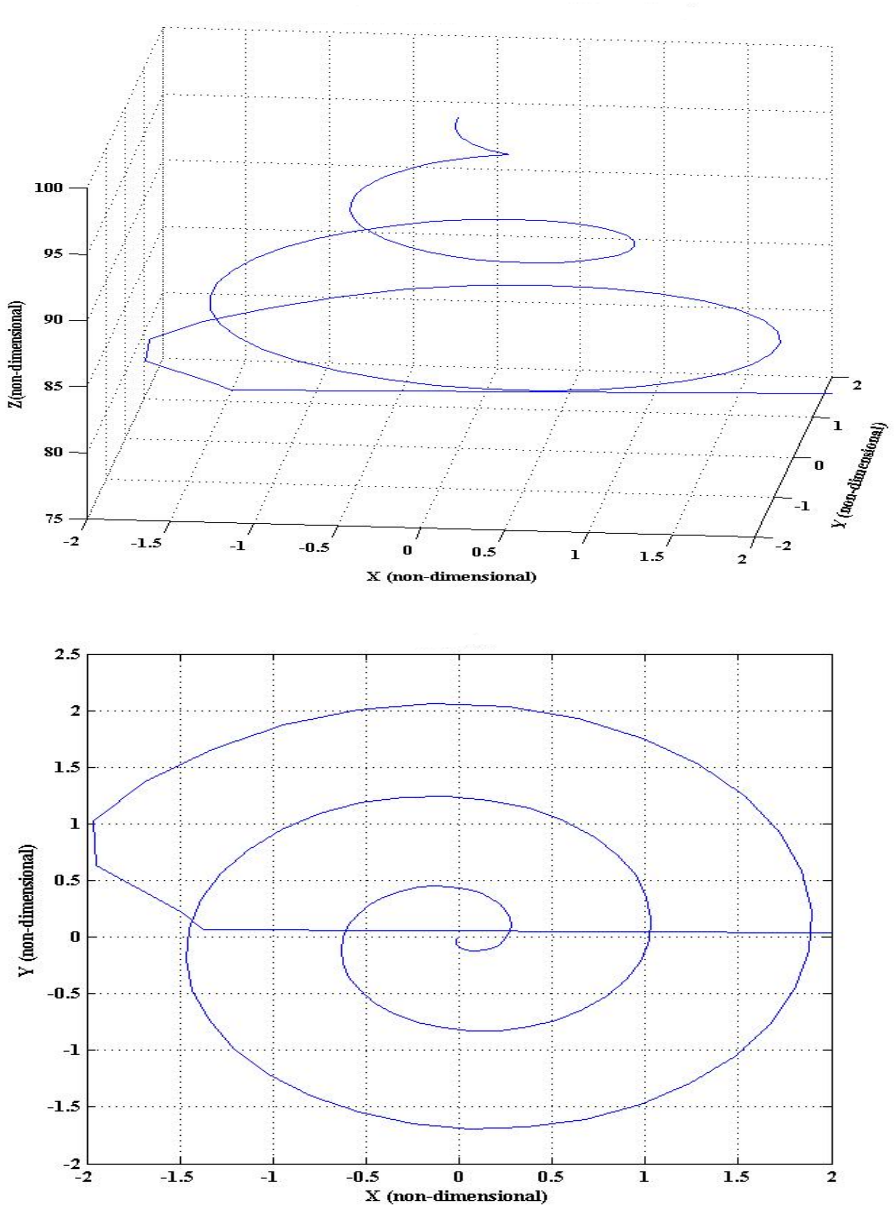

Fig. 7. Typical result for the discrete particle model showing the bending loop in the jet. Top view shows that the envelope of the jet trajectory is a cone. The number of beads for this simulation $N = 100$ and non-dimensionalized time $\bar{t} = 0.183$.

J. Results and discussion

For our initial simulations, we use the following parameter values given in [20]: initial radius a_0 is $150\mu m$, length scale L is $3.19mm$, distance between the syringe, surface tension α_0 is $0.7kg/m^2$, dynamic viscosity μ is $1000kg/(m.s)$, density ρ is $1000kg/m^3$. Based on these values the non-dimensional values used were: non-dimensional distance from syringe H is 100, dimensionless charge $Q = 12$, dimensionless Elastic modulus $F_{ve} = 12$, dimensionless voltage $V = 100$, dimensionless surface tension $A = 9$. Fig.7 shows the simulation results for this case with number of beads N being 100 and for the dimensionless time $\bar{t} = 0.179$. The 3-dimensional view shows the bending loop in the fluid jet and the top view shows the spiral formation due to electrical whipping instability as seen in experiments and prior simulation works [20, 21]. Further, our results for stresses in the fiber segments show positive values at all times. This implies that nanofibers are stretched at all times by the Coulombic interaction and the applied external field. Prior experimental works [20], have shown the formation of secondary instability with higher frequency of perturbation are formed until the jet solidifies. Our simulations do not consider solidification and so these secondary instabilities cannot be modeled in our simulations.

Comparison with existing simulations

Reneker et al. [20] have shown that using discrete bead model the values of results are far from reality unless solidification of the jet and evaporation of the solvent are considered [42]. However, the discrete bead model qualitatively gives similar results as seen in experiments. We will compare the results from our work with [20] and [21].

When we compare our results (Fig.7) at around $\bar{t} = 0.18$ to the results from [20] at similar time of $\bar{t} = 0.19$, we see that our results show more spiralling. From the

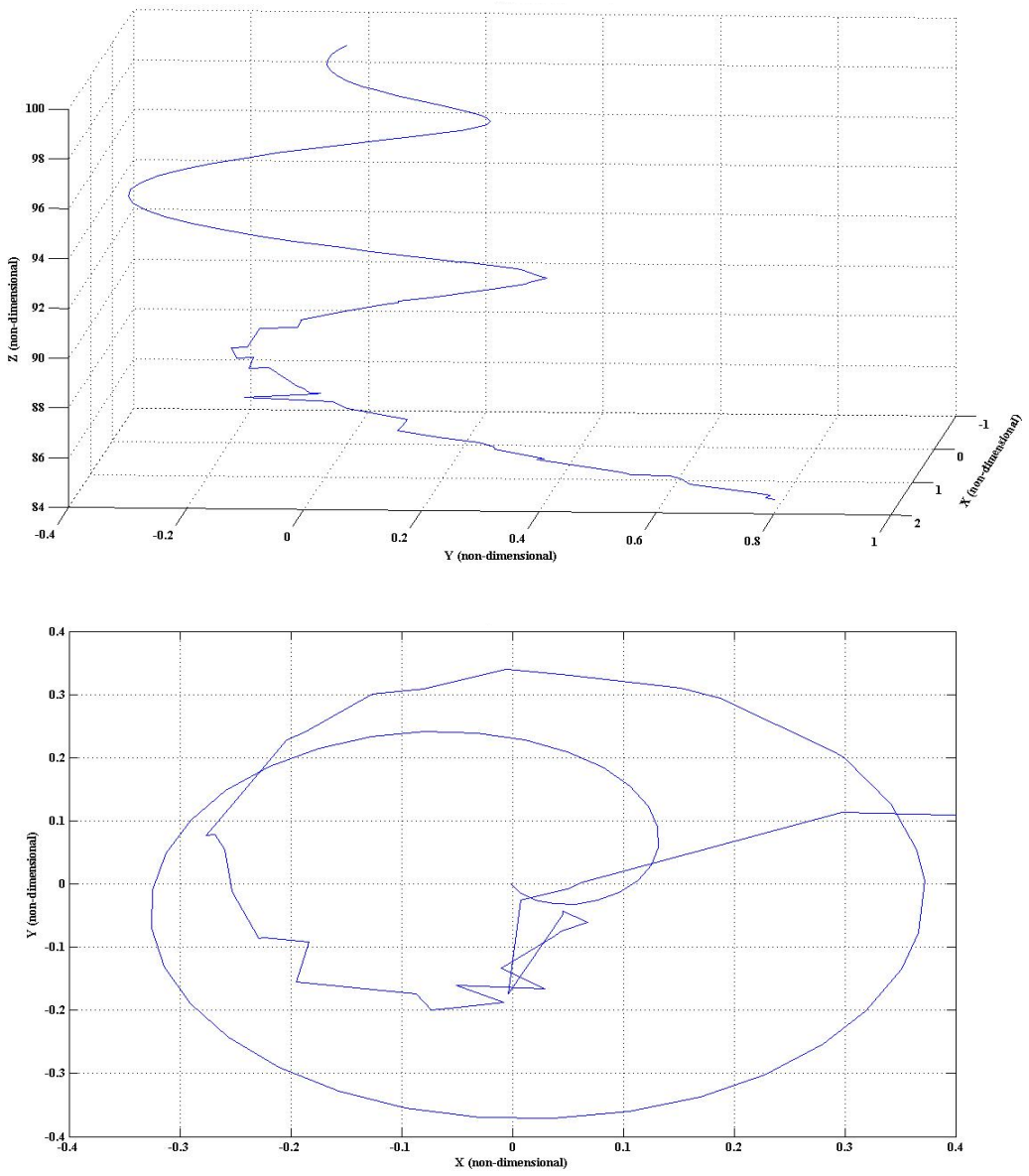

Fig. 8. 3-D view and top view for the discrete particle model when the surface tension is increased 100 times. The number of beads for this simulation $N = 100$ and dimensionless time $\bar{t} = 0.179$.

simulation in their paper [20, Fig.15], we can see that the spiralling is not smooth. In their other paper [42], localized approximation method to calculate the Coulombic interactions was developed and solidification effects were considered. The results in this paper give smoother spirals compared to the results in their first paper for whipping instability. (see [42, Fig.2]). In comparison with our current simulation (Fig.7), we can observe that our simulation (Fig.7) shows smoother spiral formation than [20, 42] and we did not consider solidification effect. This difference could be due to the change in the surface tension force calculation in our work.

Further, in our simulations, we first study the effects of surface tension. For this, we increase non-dimensional surface tension A by 100 times, keeping all the other parameters the same. Fig.8 shows the result for this case. Comparing Fig.7 and Fig.8, we see that the radii of the spirals are less when the surface tension is high. Also, comparing the top views, we see that increase in surface tension decreases the number of spirals although the distance covered in both the cases is the remains same. This means that surface tension stabilizes the jet and does not effect the vertical displacement of the jet. This observation is consistent with [20, 21].

Next, we increase the potential difference between the syringe and the collector plate 10 times and keep other parameters unchanged (see Fig.9). Comparing Fig.7 and Fig.9, we see a decrease in the radii of the when we increase the external field. Also, there is an increase in the vertical displacement of the jet when the potential difference is higher. Also, comparing the top views of Fig.7 and Fig.9, we see that the number of spirals decrease when we increase external primary field magnitude. Therefore, an increase in external potential difference stabilizes the jet. A possible explanation for this observation is as follows: As explained by Reneker et al. [20] the bending instability is mainly due to Coulombic interactions. When the external field is increased 10 times, the force due to external field dominates the Coulombic

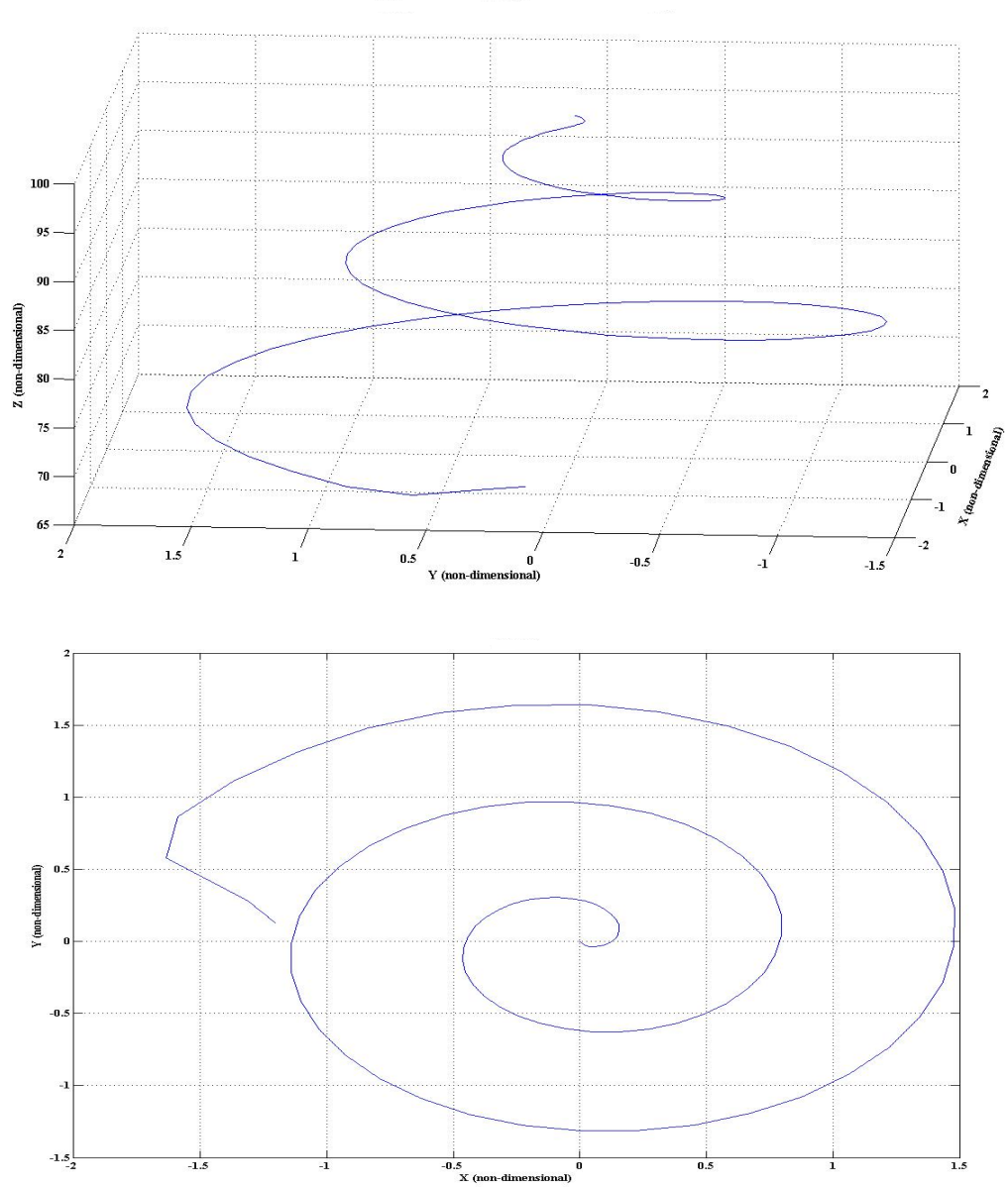

Fig. 9. 3-D view and top view for the discrete particle model when the primary field in the z-direction is increased 10 times. The number of beads for this simulation $N = 100$ and dimensionless time $\bar{t} = 0.179$.

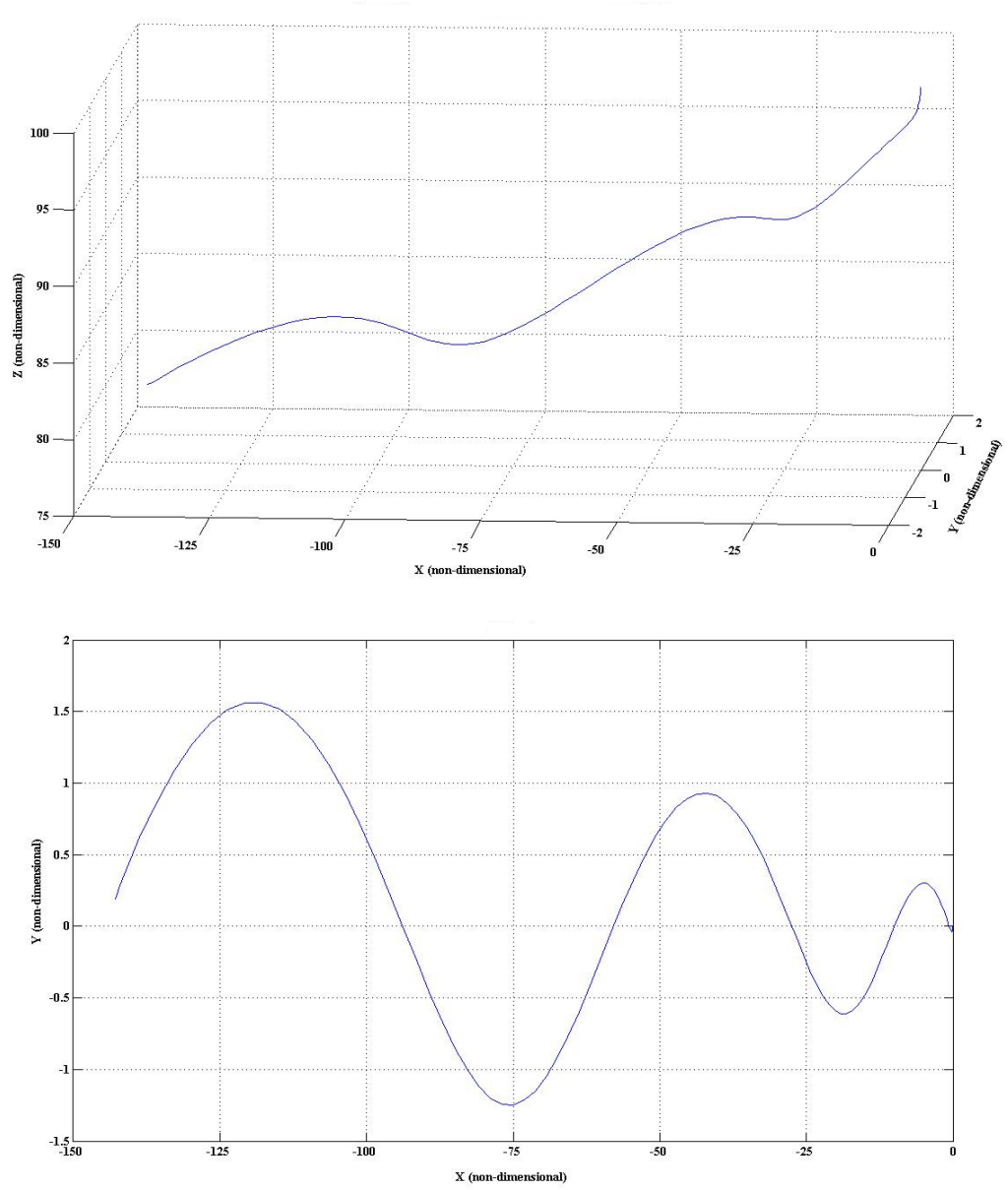

Fig. 10. 3-D view and top view for the discrete particle model when a secondary external field is applied in the x-direction which is 100 times the primary external field in z-direction. The number of beads for this simulation $N = 100$ and dimensionless time $\bar{t} = 0.179$.

interaction and so the whipping of the jet would be less compared to the distance traveled by the jet.

Effects of secondary external field

Simulations done earlier [20, 21, 42] on electrospinning have not investigated the effects of secondary external field. As discussed in previous sections, researchers have been using secondary external field to control and align the nanofibers. We discuss the effect of secondary external field, in this sub-section.

First, we apply a secondary potential difference in the negative x-direction which is 100 times the potential difference in the z-direction. All other the parameters are kept same as our initial simulation (Fig.7). Fig.10 shows the simulation results for this case. From Fig.10, we see that the spiral opens up and the fiber tranverses a distance of 150 units in the negative x-direction. We see that the vertical displacement traversed when secondary field is applied also increases (15 units without secondary field and 20 units when secondary field applied). The reason for this is as follows: When we apply secondary field, this additional electric field forces the beads to traverse further. Since, number of beads is the same in both cases (with and without secondary electric field), the total length of fiber is the same. So, the spiral opens up such that the beads can traverse more distance. Hence, this inc reases in the displacement of the fiber in the vertical and horizontal directions.

Next, we apply a secondary potential differences in the positive x-direction and in the positive y-direction which are 10 times the potential difference in the z-direction. Even in this case, see Fig.11, we see that the nanofiber spiral opens up. Due to this opening up, the fiber traverses more vertical and horizontal displacement (due to the same reason as previous case). Further, the fiber tends to travel and stretch along the line $x = y$. This direction is the direction of the secondary electric field. We further

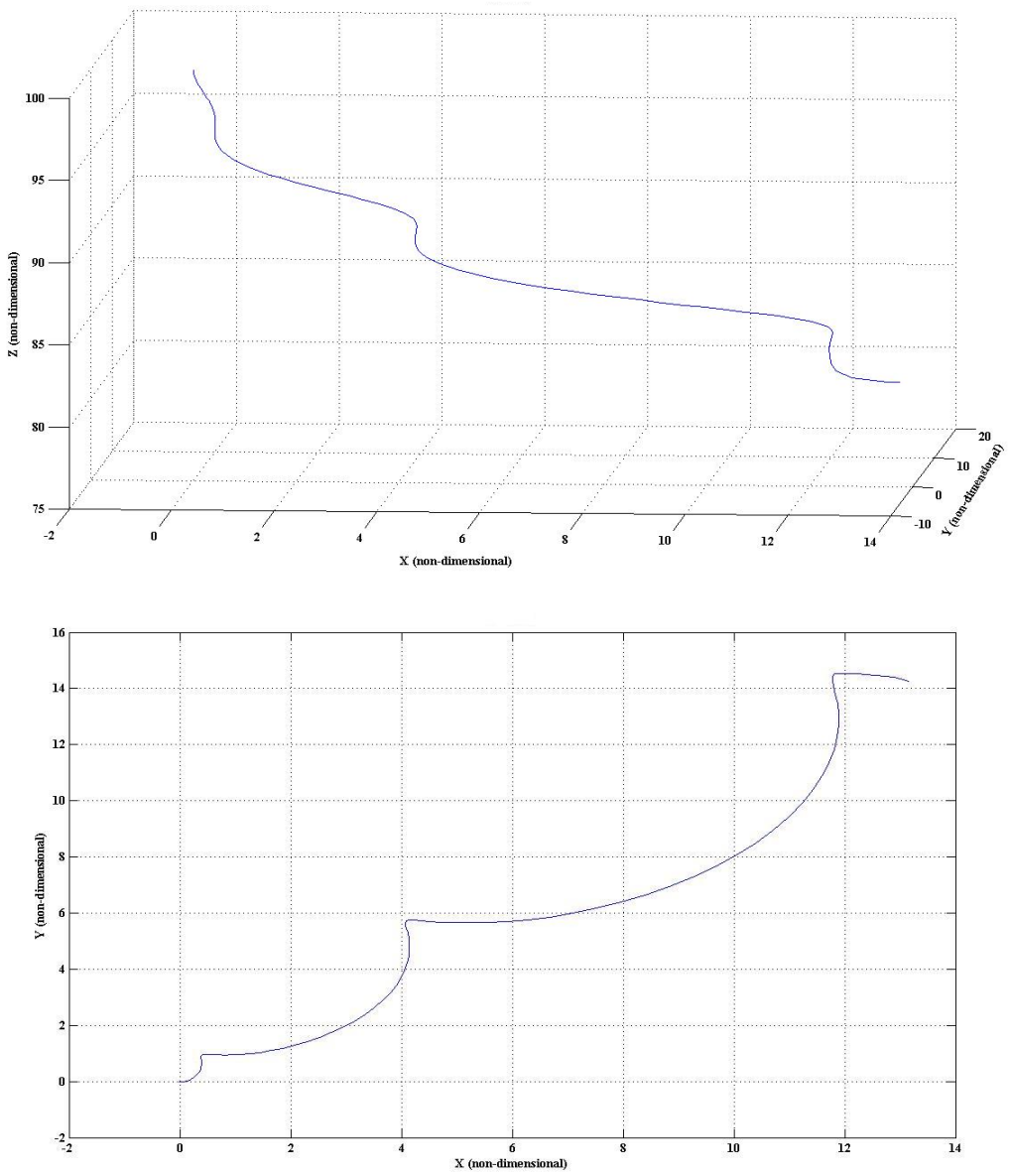

Fig. 11. 3-D view and top view for the discrete particle model when a secondary external fields are applied in the x-direction and y-direction which are 10 times the primary external field in z-direction. The number of beads for this simulation $N = 100$ and dimensionless time $\bar{t} = 0.179$.

increase in the secondary potential in the positive x-direction and in the positive y-direction to 100 times the potential difference in the z-direction. Fig.12 shows the results for this case. We observe that the fiber stretches further along the line $x = y$ and is almost parallel to $x = y$. However, the vertical displacement in this case is same as the vertical displacement when there is no secondary electric field (15 units in both cases). This is because all the opened up part of the fiber did not traverse vertically and went along the secondary field as the secondary field applied is much stronger.

One should also note that due to the application of the secondary field, there is an increase in the tension in the jet. So, the secondary field should be regulated such that the tension is not large enough to break the fiber.

K. Conclusions

In this work of thesis, we modeled a fiber as a combination of several segments with beads at the ends. We wrote the conservation of momentum for each bead which led to a system of ordinary differential equations. These equations were solved using the ODE solver in MATLAB and the spiral motion of nanofibers due to bending instability was simulated. The results were compared to prior works on electrospinning whipping instability simulations. Further, we investigated the effect of surface tension on bending instability and compared the results with prior works. Also, we studied the effect of primary external on bending instability. Finally, we looked at the effect of secondary external electric field on whipping instability. Some of the major conclusions of this work are:

- Surface tension stabilizes the jet.
- External applied primary potential difference decreases the jet spiral and in-

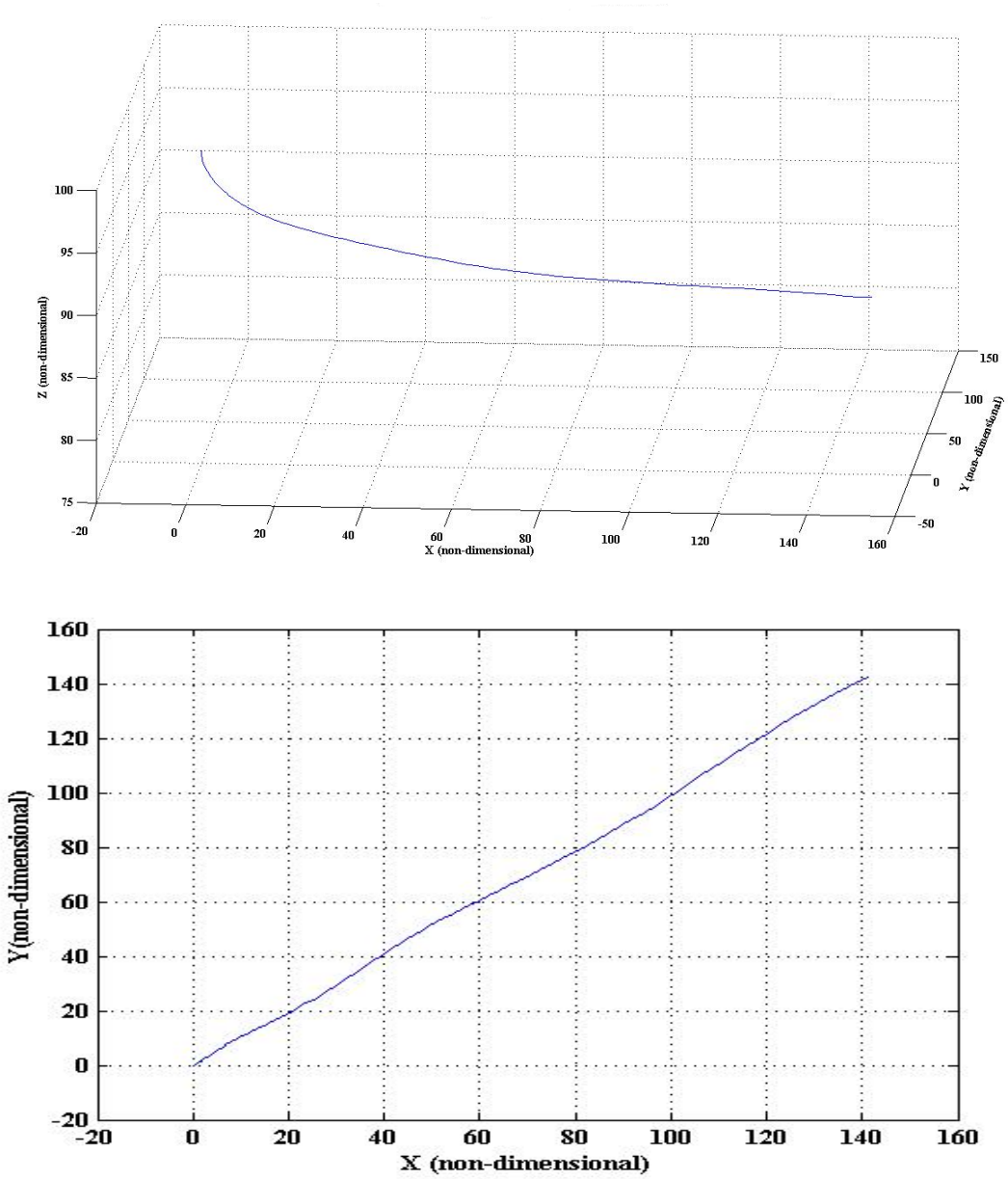

Fig. 12. 3-D view and top view for the discrete particle model when a secondary external fields are applied in the x-direction and y-direction which are 100 times the primary external field in z-direction. The number of beads for this simulation $N = 100$ and dimensionless time $\bar{t} = 0.179$.

creases the jet vertical displacement. Thereby, it stabilizes the jet.

- External applied secondary potential difference stabilizes the fiber by unwinding the spiral. This also increases the tension in the fiber.

- External applied secondary potential difference causes the jet to traverse in the direction of the resultant secondary electric field.

The last point is highly useful in controlling the motion of nanofiber. However, the secondary field increases the tension in the fiber. So, this might lead to mechanical failure in the fiber.

Recommendations for future work

The following are the recommendations for future work:

- One can investigate the effects of secondary field considering evaporation and solidification so that the results can be compared with experiments quantitatively also.

- Close to the syringe the jet is not a slender-body and the physics of the jets in the radial direction in unknown. All the works assume the jet to be slender body. One can investigate the mechanics in the radial direction which might lead to a better understanding of electrospinning jet formation.

CHAPTER III

A NUMERICAL SCHEME USING LATTICE BOLTZMANN METHOD TO SIMULATE VISCOELASTIC FLUID FLOWS

A. Introduction

Lattice Boltzmann method (LBM) has been extensively developed in the recent years as an alternate to the traditional computational techniques in CFD. LBM has proven to be a very useful method to solve flow problems involving complex fluids and complex geometries. Various problems in multi-phase flow, magnetohydrodynamics, turbulence, blood rheology, suspension flow and flow over porous media have been simulated using LBM. Mixing of two fluids between two parallel plates has been studied by Rakotomalala [43]. Denniston et al. [44] developed a numerical scheme using LBM to simulate hydrodynamics of liquid crystals. A tensorial distribution function was defined, in their method, to recover the macroscopic governing equations from the LB equation. Dupuis et al. [45] modeled droplet spreading . Dellar [46, 47] developed methods to solve problems in magnetohydrodynamics using LBM. Ladd and Verberg [14] formulated a numerical scheme based on LBM to simulate particle-fluid suspension.

Large scale complex flow problems too have been simulated as LBM codes can be parallelized. Harting et al. [13] wrote a review on large scale computations. They simulated complex fluid flows in porous media and complex fluid flows under shear in their work. LBM was found to be a faster and more effective for fluid flow simulations when compared to traditional CFD methods like finite-difference [11, 12] and spectral methods [48]. Yu et al. [49] also showed LBM to more effective compared to traditional NS solvers for solving turbulence problems.

In addition, LBM has been applied in solid mechanics. Chopard and Marconi developed LB formulation for solids in their papers [50, 51] and used this type of formulation to simulate solid-fluid interaction. Also, LBM has been extensively used in graphics and animation industry [52, 53] to simulate real life mechanics in animations.

In biomedical research, LBM had been used to simulate blood flow and blood clotting. Chin et al. [54] simulated interactions between two immiscible fluids using LBM. simulated multi-phase immiscible flow using LBM with application to blood flow. Sun and Munn simulated red blood cells flow in blood vessel using LBM. In their simulations, they used springs to model receptor- ligand bonds. Blood flow and blood clotting has been simulated by Bernsdorf et al. [55].

Aharonov and Rothman [56] made *ad hoc* modification to LBM, to simulate non-newtonian fluids. Ginzburg and Steiner [57] simulated free surface flow with Bingham fluids. They have used generalized LBE to evaluate the symmetric part of velocity gradient. Using this they have used an approach similar to Aharonov and Rothman to evaluate the viscous stress tensor. Gabbnelli et al. [58] also used LBM with *ad hoc* modifications and simulated generalized Newtonian and power law fluids. Kim et al. [59] used similar formulation to model high rate shear flow in a viscoelastic liquid bearing.

Till date, very few methods have been developed using LBM to solve viscoelasticity. Ispolatov and Grant [60] developed a LBM which uses Maxwell's linear model. In their method, they have considered Maxwell's elastic stress as an external body force. Lallemand et al. [61] formulated a multiple relaxation technique to model viscoelastic fluid. Qian and Deng [16] introduced an extra term in the equilibrium distribution function which models the elastic component. These three models above models do not consider the advection of the viscoelastic stress. Such models can only be used for small deformations (see [5]) and hence these methods [60, 61, 16] are not

applicable for polymer fluids flows, where the deformations are large.

Giraud et al. [17] proposed a entirely mesoscopic based formulation with multiple relaxation times and have recovered the Jeffrey's equation using Chapman-Enskog method. Giupponi et al. [62] proposed a purely kinetic approach to simulate gyroid mesophases and have shown that their method could be used to simulate viscoelastic flow problems. In these two works, the advection of viscoelastic stress tensor have been considered and hence correctly model viscoelastic fluid flows. Ahlrichs et al. [63] established a method which couples lattice Boltzmann method for the fluid with a molecular dynamics model for polymer chain. An external forcing term which models the solvent-polymer interaction is introduced in the LB formulation.

In this chapter, we develop macroscopic based formulation which couples LBM with finite difference. This chapter is organized as follows: In section B, the lattice Boltzmann method is briefly described. The continuum governing equations for viscoelastic polymer solution that follows Oldroyd-B constitutive model is presented in section C. The numerical method and its validation are discussed in sections D and E respectively. In section F, we summarize and conclude the chapter.

B. Lattice Boltzmann method

The lattice Boltzmann equation using single relaxation time approximation based on BGK collision operator is given by

$$f_\alpha(\mathbf{x}+\mathbf{e}_\alpha, t+1) - f_\alpha(\mathbf{x}, \mathbf{t}) = -\frac{1}{\tau}(f_\alpha - f_\alpha^{eq}) \tag{3.1}$$

where f_α is the density distribution along the direction $\mathbf{e}_\alpha$, f_α^{eq} is the equilibrium density distribution along the direction $\mathbf{e}_\alpha$, τ is the relaxation time of collision. (For theory of the Boltzmann equation, see [64, 65]. For the derivation of lattice Boltzmann

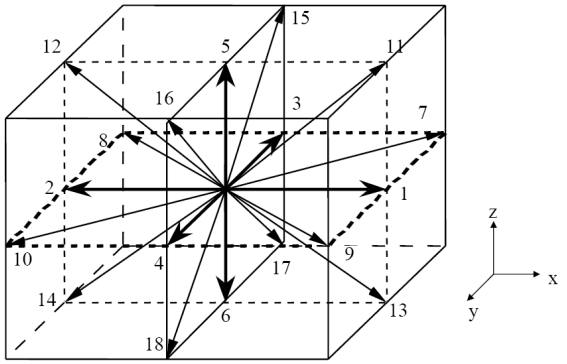

Fig. 13. *D3Q19* lattice

equation from the Boltzmann equation, see [66].) In our work, we use the D3Q19 (see Fig.13) lattice, which has 19 velocities in 3 dimensions. The discrete velocities in this case are:

$$\mathbf{e}_\alpha = \begin{cases} (0,0,0)c & \alpha = 0 \\ (\pm 1,0,0)c, (0,\pm,0)c, (0,0,\pm)c & \alpha = 1,2,\cdots,6 \\ (\pm 1,\pm 1,0)c, (\pm 1,0,\pm 1)c, (\pm 1,\pm 1,0)c & \alpha = 7,8,\cdots,18 \end{cases} \tag{3.2}$$

The equilibrium distribution for can be given by

$$f_\alpha^{eq} = w_\alpha \rho \left(1 + \frac{1}{3}\mathbf{e}_\alpha \cdot \mathbf{u} + \frac{9}{2}(\mathbf{e}_\alpha \cdot \mathbf{u})^2 - \frac{3}{2}\mathbf{u} \cdot \mathbf{u}\right) \tag{3.3}$$

where ρ is the density, $c = \delta_x/\delta_t$ with δ_x being the lattice constant and δ_t being the time step, w_α are the weights given by $w_0 = 1/3$, $w_{1-6} = 1/18$, $w_{7-18} = 1/36$ for a *D3Q19* lattice, and $\mathbf{u}$ is the velocity vector. The speed of sound of the model is

$c_s = c/\sqrt{3}$ Equation (3.3) can be re-written for an incompressible flow as:

$$f_\alpha^{eq} = w_\alpha \left[\delta\rho + \rho_0 \left(\frac{1}{3}\mathbf{e}_\alpha \cdot \mathbf{u} + \frac{9}{2}(\mathbf{e}_\alpha \cdot \mathbf{u})^2 - \frac{3}{2}\mathbf{u} \cdot \mathbf{u} \right) \right] \tag{3.4}$$

where $\delta\rho$ is the fluctuation in the density and ρ_0 is the constant mean density within the system, which is usually set to 1. c is also usually set to 1. With the conservation of mass and momentum given by:

$$\delta\rho = \sum_\alpha f_\alpha = \sum_\alpha f_\alpha^{eq} \tag{3.5}$$

$$\rho_0 \mathbf{u} = \sum_\alpha \mathbf{e}_\alpha f_\alpha = \sum_\alpha \mathbf{e}_\alpha f_\alpha^{eq} \tag{3.6}$$

The momentum flux $\mathbf{\Pi}$ can be given by the second moment of the distribution function f_α, as follows:

$$\mathbf{\Pi} = \sum_\alpha \mathbf{e}_\alpha \mathbf{e}_\alpha f_\alpha = \rho \mathbf{u}\mathbf{u} + p\mathbf{I} = \rho \mathbf{u}\mathbf{u} + \frac{\rho}{c_s^2}\mathbf{I} \tag{3.7}$$

Using multi-scale Chapman-Enskog procedure on Equation (3.1), the following hydrodynamic equations can be derived

$$\frac{\partial \rho}{\partial t} + \nabla \rho \mathbf{u} = 0 \tag{3.8}$$

$$\frac{\partial \mathbf{u}}{\partial t} + (\nabla \mathbf{u})\mathbf{u} = -\nabla p + \nabla^2 \mathbf{u} \tag{3.9}$$

where $p = c_s^2 \rho/\rho_0$ and the kinematic viscosity (ν) can be related to the relaxation time as $\tau = \frac{1}{3}(\nu - \frac{1}{2})$. Further, while recovering the hydrodynamic equations, one can see that the symmetric part of the velocity gradient $\mathbf{D}$ for the incompressible viscous fluid can be given by [65]

$$\mathbf{D}_{ij} = \frac{1}{2}\left(\frac{\partial u_i}{\partial x_j} + \frac{\partial u_j}{\partial x_i} \right) = -\frac{1}{2\rho_0 c_s^2 \tau} \sum_\alpha e_{\alpha i} e_{\alpha j} [f_\alpha - f_\alpha^{eq}] \tag{3.10}$$

C. Continuum equations for viscoelastic fluids

Assuming that the fluid is incompressible, the continuum/macroscopic governing equations for the problem are given by

$$div\mathbf{u} = 0 \tag{3.11}$$

$$\rho\left[\frac{\partial \mathbf{u}}{\partial t} + (\nabla \mathbf{u})\mathbf{u}\right] = div\sigma + \rho\mathbf{b} \tag{3.12}$$

where ρ is the density of jet fluid, $\mathbf{u}$ is the velocity field vector, div is the divergence operator, $\mathbf{b}$ is the body force and the Cauchy stress tensor σ is given by

$$\sigma = -p\mathbf{I} + \mathbf{T}' \tag{3.13}$$

In our work, we consider only a polymer solution. The stress tensor $\mathbf{T}'$ corresponds to the hydrodynamics stresses within a polymer solution which constitutes of a solvent and polymer.

$$\mathbf{T}' = 2\eta_2\mathbf{D} + \mathbf{T} \tag{3.14}$$

The first part on the right side of Eq.(8) models the solvent of the solvent-polymer solution with η_2 being the solvent viscosity. The tensor $\mathbf{T}$ models the polymer which is the Non-newtonian part of the solvent-polymer solution mixture which evolves as

$$\mathbf{T} + \lambda\left(\frac{D\mathbf{T}}{Dt}\right) = 2\eta_1\mathbf{D} \tag{3.15}$$

Equation (3.15) is Upper Convected Maxwell model for viscoelasticity, where λ is the relaxation time and η_1 the viscosity. $\mathbf{D}$ is the symmertric part of the Eulerian velocity

gradient given by

$$\mathbf{D} = \frac{1}{2}(\mathbf{L} + \mathbf{L}^T) \tag{3.16}$$

where $\mathbf{L} = \nabla\mathbf{u}$, is the Eulerian velocity gradient and $\mathbf{L}^T$ is the transpose of $\mathbf{L}$. Also,

$$\frac{D\mathbf{T}}{Dt} = \frac{\partial\mathbf{T}}{\partial t} + [\text{grad}\mathbf{T}]\mathbf{u} - \mathbf{L}\mathbf{T} - \mathbf{T}\mathbf{L}^T \tag{3.17}$$

Now, combining equations (3.14) and (3.15) we get

$$\mathbf{T}' + \lambda\left(\frac{D\mathbf{T}'}{Dt}\right) = 2\left[(\eta_1 + \eta_2)\mathbf{D} + \lambda\eta_2\left(\frac{D\mathbf{D}}{Dt}\right)\right] \tag{3.18}$$

This is same as Oldroyld-B model for viscoelastic polymer solutions (see [5]) usually given by

$$\mathbf{T}' + \lambda_1\left(\frac{D\mathbf{T}'}{Dt}\right) = 2\eta\left[\mathbf{D} + \lambda_2\left(\frac{D\mathbf{D}}{Dt}\right)\right] \tag{3.19}$$

Comparing equations (3.18) and (3.19), we can see that

$$\eta = \eta_1 + \eta_2 \tag{3.20}$$

and

$$\frac{\lambda_2}{\lambda_1} = \frac{\eta_2}{\eta_1 + \eta_2} \tag{3.21}$$

D. Numerical scheme

Dellar in his paper [47] showed that the addition in the equilibrium distribution ($\triangle f_\alpha^{eq}$) due to the change in the Cauchy stress tensor $\triangle\sigma$ is

$$\triangle f_\alpha^{eq} = -\frac{w_\alpha}{2c_s^2}\left[(\mathbf{e}_\alpha\mathbf{e}_\alpha - \frac{1}{3}\mathbf{I}) : (-\triangle\sigma - \frac{1}{3}(Tr(-\triangle\sigma))\mathbf{I})\right] \tag{3.22}$$

In our case, for viscoelastic polymer solution from equation (3.13), we have $\triangle\sigma = \mathbf{T}$ The equilibrium distribution equation, after adding the terms due to viscoelastic

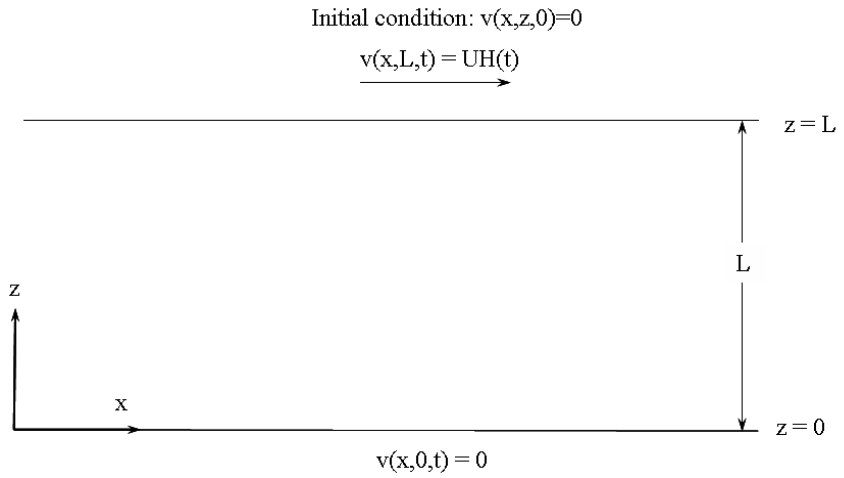

Fig. 14. Schematic showing start-up Couette flow. The lower plate is at rest at all times while the upper plate moves with a constant velocity 'U', H(t) is the heaviside function.

stress tensor, is given by

$$\begin{aligned} f_\alpha^{eq} = w_\alpha \left[\delta\rho + \rho_0 \left(\frac{1}{3}\mathbf{e}_\alpha \cdot \mathbf{u} + \frac{9}{2}(\mathbf{e}_\alpha \cdot \mathbf{u})^2 - \frac{3}{2}\mathbf{u}\cdot\mathbf{u}\right)\right] \\ - \frac{9}{2}w_\alpha \mathbf{e}_{\alpha i}\mathbf{e}_{\alpha j}\mathbf{T}_{ji} - \frac{3}{2}w_\alpha \left(\frac{D}{3} - 1 - |\mathbf{e}_\alpha|^2\right)\mathbf{T}_{ii} \end{aligned} \tag{3.23}$$

where D is the number of dimensions of space in the problem. We use three dimensional space ($D = 3$) for our problem. Hence, equation (3.23) will reduce to

$$\begin{aligned} f_\alpha^{eq} = w_\alpha \left[\delta\rho + \rho_0 \left(\frac{1}{3}\mathbf{e}_\alpha \cdot \mathbf{u} + \frac{9}{2}(\mathbf{e}_\alpha \cdot \mathbf{u})^2 - \frac{3}{2}\mathbf{u}\cdot\mathbf{u}\right)\right] \\ - \frac{9}{2}w_\alpha \mathbf{e}_{\alpha i}\mathbf{e}_{\alpha j}\mathbf{T}_{ji} + \frac{3}{2}w_\alpha |\mathbf{e}_\alpha|^2\mathbf{T}_{ii} \end{aligned} \tag{3.24}$$

Now, applying forward step finite difference method in time to equation (3.15), we get

$$\mathbf{T}(t+\triangle t) = \left(1 - \frac{\triangle t}{\lambda}\right)\mathbf{T}(t) + 2\eta_1 \triangle t \mathbf{D}/\lambda - (\triangle t)[(\mathrm{grad}\mathbf{T})\mathbf{u} - \mathbf{L}\mathbf{T} - \mathbf{T}\mathbf{L}^T] \tag{3.25}$$

where $\triangle t$ is the time step.

To solve a flow problem with Oldroyd-B fluid, we propose the following algorithm for a given domain:
First, define a scalar distribution function (f) and define the initial conditions for ρ, $\mathbf{u}$, $\mathbf{T}$. For time varying from initial time to final time

1. Evaluate the equilibrium distribution function using equation (3.24).
2. Using equation (3.1), evaluate the distribution function after 1 lattice time step and also apply the boundary conditions. Also evaluate $\mathbf{D}$ using equation (3.10).
3. Evaluate the macroscopic quantities $\mathbf{u}$, ρ at new time step using equations (3.5) and (3.6). Evaluate $\mathbf{L}$ using central difference in lattice space.
4. Update the viscoelastic extra stress tensor ($\mathbf{T}$) using equation (3.25). Note that the properties η, λ should be converted to lattice units.
5. Go to step 1.

E. Validation of the method

Tome et al. [9] validated their finite difference approach for Oldroyd-B fluid flows using start-up Couette flow. Mompean et al. [8] also validated their finite difference method for simulating Oldroyd-B fluid flows using start-up Couette flow. We also simulate the start-up Couette flow for an Oldroyd-B polymer solution and compare our results with the analytical results available in literature [9, 69].

Fig.14 shows the schematic for start-up Couette flow. The bottom plate is at rest for all time while the upper plate is moved from rest to velocity U at time $t = 0$.

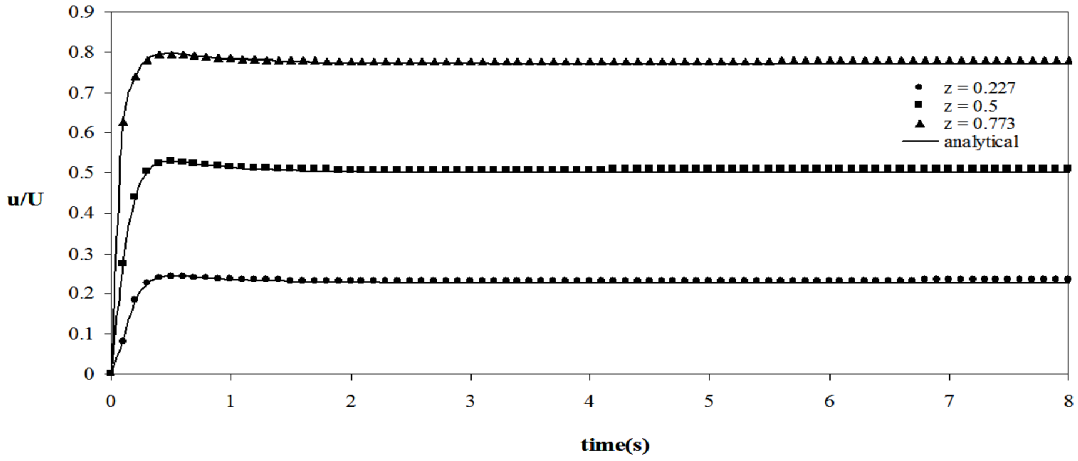

Fig. 15. Comparison of the non-dimensionalized velocity ($\mathbf{u/U}$) growth between analytical [9, 69] and numerical results with $\eta_1 = \eta_2 = 1$ in a start-up Couette flow for Reynolds number $Re = 0.5$, Weissenberg number $We = 1.1$. Three points at $z = 0.227\text{L}, z = 0.5\text{L}, z = 0.772\text{L}$ where chosen with L = 1 (see Fig.14) and the total time is $8s$.

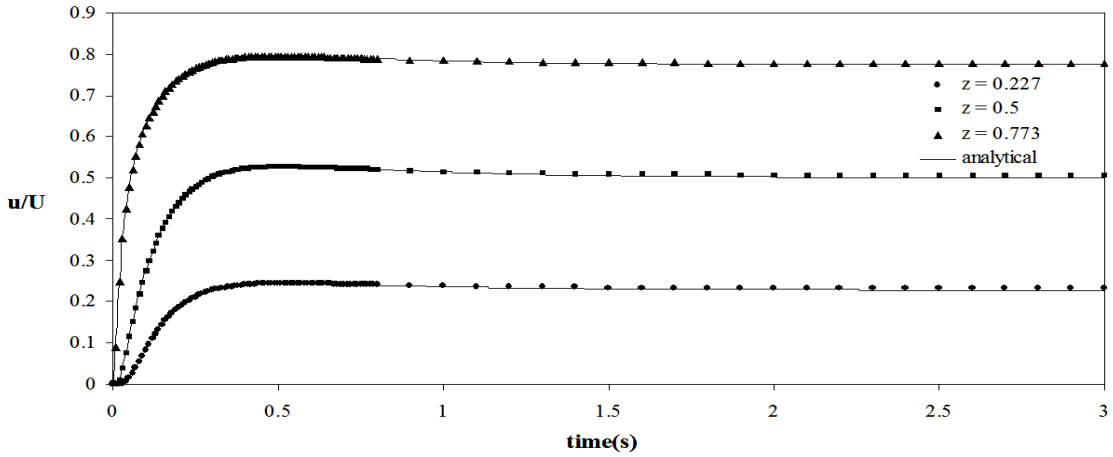

Fig. 16. Comparison of the non-dimensionalized velocity ($\mathbf{u/U}$) growth between analytical [9, 69] and numerical results with $\eta_1 = \eta_2 = 1$ in a start-up Couette flow for Reynolds number $Re = 0.5$, Weissenberg number $We = 1.1$. Three points at $z = 0.227\text{L}, z = 0.5\text{L}, z = 0.772\text{L}$ where chosen with L = 1 (see Fig.14). Total time chosen is $3s$ to get a closer view at the velocity growths.

Following above two papers [8, 9], we observe the velocity evolution at three points in the z-direction. We choose $z = 0.227\text{L}, z = 5\text{L}, z = 0.772\text{L}$ as our three points. For our simulation we assume, $\lambda = 1.1$, $L = 1$, $\rho = 1$ and $\eta_2 = 1$. We also set $\eta_2 = \eta_1$. So, from equation (3.20), we get $\eta = 2$ and from equation (3.21), we get $\lambda_2/\lambda_1 = 0.5$. Also, we get Reynolds number, as $Re = \rho\text{L}/\eta = 0.5$ and Weissenberg number as $We = \lambda U/\text{L} = 1.1$. We choose a 11×200 inner grid with two extra nodes for the top and bottom walls. The spatial lattice unit would be $\delta x = 0.909$ and we choose lattice unit for time to be $\delta t = 0.001$.

From this we get, $c = 90.0$ and $U = 0.01$, in lattice units. Notice that Mach number $M = \sqrt{3}U/c \ll 0.1$. Assuming $\rho = 1$ for the lattice space, the kinematic viscosity in lattice units is $\nu = 0.121$. This leads to $\tau = 0.863$ and $\lambda = 1100$ in lattice

units. Also, in our simulations we use bounce-back condition [67] for the top plate which is equivalent to no slip condition with boundary at rest. For the top, we use the bounce-back condition [67] for moving wall. For the left-most and right-most ends we used extrapolation boundary conditions [67, 68]. We run the simulation for 8000 lattice time units which is equivalent to 8s.

Fig.15 shows the velocity growth comparison between the analytical results and numerical results for total time of 8s. To get a better look at the transient part, we compare the velocity data for first $3s$. Fig.16 shows the velocity growth comparison between the analytical results and numerical results for first $3s$. From Fig.15 and Fig.16, we see that the simulation velocities match well with analytical values, for both transient state and steady state. We also check the viscoelastic extra stress data ($\mathbf{T_{xz}}$) from our simulations with the analytical solution [9, 69]. Even the viscoelastic extra stresses match very well with the analytical values (see Fig.17).

F. Conclusions and future work

We proposed lattice Boltzmann method based numerical scheme. This method couples lattice Boltzmann method with finite difference method for a Oldroyd-B viscoelastic solution. The extra stress tensor due to polymer viscoelasticity was included in the equilibrium distribution function and the distribution function was updated using SRT model. Then, local velocities were calculated from the distribution function. Velocities calculated in this manner were used to evaluate local velocity gradients and local symmetric part of the velocity gradients using central difference method. Using a forward difference scheme in time on the Oldroyd-B constitutive equation, the viscoelastic stress tensor was updated. Finally, we validated the numerical method by solving start-up Couette flow problem, which has been used as a benchmark problem

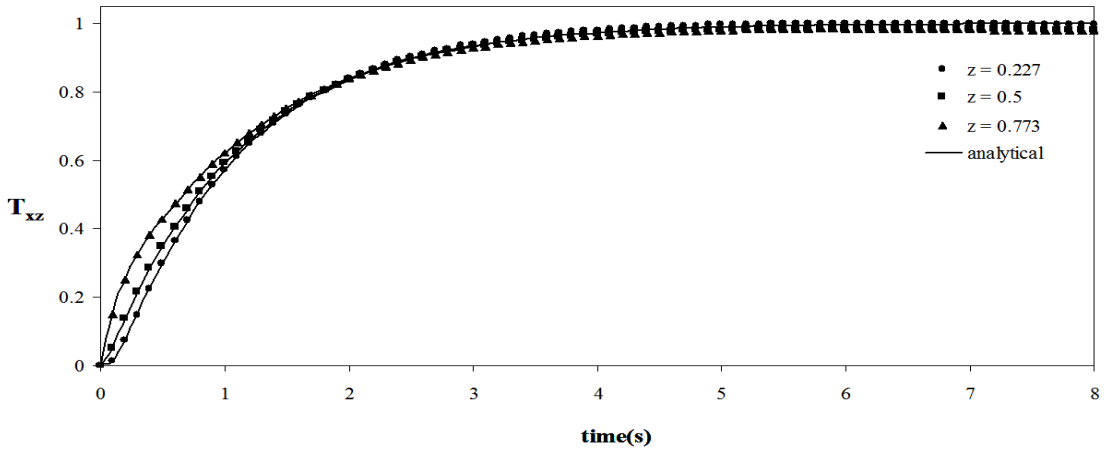

Fig. 17. Comparison of the viscoelastic extra stress ($\mathbf{T_{xz}}$) growths between analytical and numerical results with $\eta_1 = \eta_2 = 1$ in a start-up Couette flow with Reynolds number $Re = 0.5$, Weissenberg number $We = 1.1$. Three points at $z = 0.227\mathrm{L}, z = 0.5\mathrm{L}, z = 0.772\mathrm{L}$ where chosen with $\mathrm{L} = 1$ (see Fig.14). Total time shown is $8s$.

in literature for viscoelastic solutions.

This method can be used to study flow problems like die-swell extrusion, jet buckling and jet formation in classical spinning process with polymer solutions. One must note that our method can be used for only a polymer solution and cannot be implemented for polymer melt flow problems like melt-spinning. Also, since this method uses finite difference, any small errors may get propagated.

CHAPTER IV

SUMMARY

In this thesis, we first looked at the jet flow problem in electrospinning process. We formulated our work based on discrete bead model. We compared our results with simulation works in literature. We found our results to be consistent with these studies. Also, using our code, we simulated the effect of external secondary field on the jet flow and jet instability. We found that the external secondary field reduces the whipping instability. We also observed that whipping jet spiral unwound in the direction of the resultant secondary field.

Next, in the latter part of the thesis, we developed a hybrid numerical scheme with LBM and finite difference for an Oldroyd-B polymer solution. We also validated the method by simulating the start-up Couette flow problem, which has been used as a benchmark problem in literature. For our simulations, we used $Re = 0.5$ and $We = 1.1$.

REFERENCES

[1] M. M. Denn, "Issues in viscoelastic fluid-mechanics," *Annual Review of Fluid Mechanics*, vol. 22, pp. 13–34, 1990.

[2] A. R. Srinivasa, "Flow characteristics of a "multiconfigurational", shear thinning viscoelastic fluid with particular reference to the orthogonal rheometer," *Theoretical and Computational Fluid Dynamics*, vol. 13, pp. 305–325, Feb. 2000.

[3] K. Kannan and K. R. Rajagopal, "Simulation of fiber spinning including flow-induced crystallization," *Journal of Rheology*, vol. 49, pp. 683–703, May–Jun. 2005.

[4] S. E. Bechtel, M. G. Forest, and D. B. Bogy, "A one-dimensional theory for viscoelastic fluid jets, with application to extrudate swell and draw-down under gravity," *Journal of Non-Newtonian Fluid Mechanics*, vol. 21, pp. 273–308, Aug. 1986.

[5] R. B. Bird, *Dynamics of polymeric liquids*, 2nd ed. New York, NY: Wiley, 1987.

[6] Z. M. Huang, Y. Z. Zhang, M. Kotaki, and S. Ramakrishna, "A review on polymer nanofibers by electrospinning and their applications in nanocomposites," *Composites Science and Technology*, vol. 63, pp. 2223–2253, Nov. 2003.

[7] W. E. Teo and S. Ramakrishna, "A review on electrospinning design and nanofibre assemblies," *Nanotechnology*, vol. 17, pp. R89–R106, Jul. 2006.

[8] G. Mompean and M. Deville, "Unsteady finite volume simulation of Oldroyd-B fluid through a three-dimensional planar contraction," *Journal of Non-Newtonian Fluid Mechanics*, vol. 72, pp. 253–279, Oct. 1997.

[9] M. F. Tome, N. Mangiavacchi, J. A. Cuminato, A. Castelo, and S. McKee, "A finite difference technique for simulating unsteady viscoelastic free surface flows," *Journal of Non-Newtonian Fluid Mechanics*, vol. 106, pp. 61–106, Sep. 2002.

[10] F. P. T. Baaijens, "Mixed finite element methods for viscoelastic flow analysis: a review," *Journal of Non-Newtonian Fluid Mechanics*, vol. 79, pp. 361–385, Nov. 1998.

[11] A. J. C. Ladd, "Numerical simulations of particulate suspensions via a discretized Boltzmann-equation .1. theoretical foundation," *Journal of Fluid Mechanics*, vol. 271, pp.285–309, Jul. 1994.

[12] A. J. C. Ladd, "Numerical simulations of particulate suspensions via a discretized Boltzmann-equation .2. numerical results," *Journal of Fluid Mechanics*, vol. 271, pp. 311–339, Jul. 1994.

[13] J. Harting, J. Chin, M. Venturoli, and P. V. Coveney, "Large-scale lattice Boltzmann simulations of complex fluids: advances through the advent of computational Grids," *Philosophical Transactions of the Royal Society A–Mathematical Physical and Engineering Sciences*, vol. 363, pp. 1895–1915, Aug. 2005.

[14] A. J. C. Ladd and R. Verberg, "Lattice-Boltzmann simulations of particle-fluid suspensions," *Journal of Statistical Physics*, vol. 104, pp. 1191–1251, Sep. 2001.

[15] P. Lallemand and L. S. Luo, "Lattice Boltzmann method for moving boundaries," *Journal of Computational Physics*, vol. 184, pp. 406–421, Jan. 2003.

[16] Y. H. Qian and Y. F. Deng, "A lattice BGK model for viscoelastic media," *Physical Review Letters*, vol. 79, pp. 2742–2745, Oct. 1997.

[17] L. Giraud, D. D'Humieres, and P. Lallemand, "A lattice Boltzmann model for Jeffrey's viscoelastic fluid," *Europhysics Letters*, vol. 42, pp. 625–630, Jun. 1998.

[18] Z. Huang, H. C. Chen, Z. K. Chen, and M. C. Roco, "International nanotechnology development in 2003: country, institution, and technology field analysis based on USPTO patent database," *Journal of Nanoparticle Research*, vol. 6, pp. 325–354, Aug. 2004.

[19] S. Ramakrishna, *An introduction to electrospinning and nanofibers*. Hackensack, NJ: World Scientific, 2005.

[20] D. H. Reneker, A. L. Yarin, H. Fong, and S. Koombhongse, "Bending instability of electrically charged liquid jets of polymer solutions in electrospinning," *Journal of Applied Physics*, vol. 87, pp. 4531–4547, May 2000.

[21] T. A. Kowalewski, S. Blonski, and S. Barral, "Experiments and modelling of electrospinning process," *Bulletin of the Polish Academy of Sciences*, vol. 53, pp. 385–394, 2005.

[22] T. Ondarcuhu and C. Joachim, "Drawing a single nanofibre over hundreds of microns," *Europhysics Letters*, vol. 42, pp. 215–220, Apr. 1998.

[23] C. R. Martin, "Membrane-based synthesis of nanomaterials," *Chemistry of Materials*, vol. 8, pp. 1739–1746, Aug. 1996.

[24] P. X. Ma and R. Y. Zhang, "Synthetic nano-scale fibrous extracellular matrix," *Journal of Biomedical Materials Research*, vol. 46, pp. 60–72, Jul. 1999.

[25] Y. Z. Zhang, C. T. Lim, S. Ramakrishna, and Z. M. Huang, "Recent development of polymer nanofibers for biomedical and biotechnological applications," *Journal of Materials Science-Materials in Medicine*, vol. 16, pp. 933–946, Oct. 2005.

[26] G. M. Whitesides and B. Grzybowski, "Self-assembly at all scales," *Science*, vol. 295, pp. 2418–2421, Mar. 2002.

[27] J. D. Hartgerink, J. R. Granja, R. A. Milligan, and M. R. Ghadiri, "Self-assembling peptide nanotubes," *Journal of the American Chemical Society*, vol. 118, pp. 43–50, Jan. 1996.

[28] X. Y. Wang, C. Drew, S. H. Lee, K. J. Senecal, J. Kumar, and L. A. Sarnuelson, "Electrospun nanofibrous membranes for highly sensitive optical sensors," *Nano Letters*, vol. 2, pp. 1273–1275, Nov. 2002.

[29] R. Dersch, M. Steinhart, U. Boudriot, A. Greiner, and J. H. Wendorff, "Nanoprocessing of polymers: applications in medicine, sensors, catalysis, photonics," *Polymers for Advanced Technologies*, vol. 16, pp. 276–282, Feb.–Mar. 2005.

[30] G. Taylor, "Disintegration of water drops in electric field," *Proceedings of the Royal Society of London Series A–Mathematical and Physical Sciences*, vol. 280, pp. 383–397, 1964.

[31] A. L. Yarin, S. Koombhongse, and D. H. Reneker, "Taylor cone and jetting from liquid droplets in electrospinning of nanofibers," *Journal of Applied Physics*, vol. 90, pp. 4836–4846, Nov. 2001.

[32] J. Doshi and D. H. Reneker, "Electrospinning process and applications of electrospun fibers," *Journal of Electrostatics*, vol. 35, pp. 151–160, Aug. 1995.

[33] Y. M. Shin, M. M. Hohman, M. P. Brenner, and G. C. Rutledge, "Experimental characterization of electrospinning: the electrically forced jet and instabilities," *Polymer*, vol. 42, pp. 9955–9967, Dec. 2001.

[34] A. Jaworek and A. Krupa, "Classification of the modes of EHD spraying," *Journal of Aerosol Science*, vol. 30, pp. 873–893, Aug. 1999.

[35] M. M. Hohman, M. Shin, G. Rutledge, and M. P. Brenner, "Electrospinning and electrically forced jets. I. stability theory," *Physics of Fluids*, vol. 13, pp. 2201–2220, Aug. 2001.

[36] M. M. Hohman, M. Shin, G. Rutledge, and M. P. Brenner, "Electrospinning and electrically forced jets. II. applications," *Physics of Fluids*, vol. 13, pp. 2221–2236, Aug. 2001.

[37] T. Subbiah, G. S. Bhat, R. W. Tock, S. Pararneswaran, and S. S. Ramkumar, "Electrospinning of nanofibers," *Journal of Applied Polymer Science*, vol. 96, pp. 557–569, Apr. 2005.

[38] S. A. Theron, A. L. Yarin, E. Zussman, and E. Kroll, "Multiple jets in electrospinning: experiment and modeling," *Polymer*, vol. 46, pp. 2889–2899, Apr. 2005.

[39] D. Li, Y. L. Wang, and Y. N. Xia, "Electrospinning of polymeric and ceramic nanofibers as uniaxially aligned arrays," *Nano Letters*, vol. 3, pp. 1167–1171, Aug. 2003.

[40] J. J. Feng, "Stretching of a straight electrically charged viscoelastic jet," *Journal of Non-Newtonian Fluid Mechanics*, vol. 116, pp. 55–70, Dec. 2003.

[41] J. J. Feng, "The stretching of an electrified non-Newtonian jet: a model for electrospinning," *Physics of Fluids*, vol. 14, pp. 3912–3926, Nov. 2002.

[42] A. L. Yarin, S. Koombhongse, and D. H. Reneker, "Bending instability in electrospinning of nanofibers," *Journal of Applied Physics*, vol. 89, pp. 3018–3026,

Mar. 2001.

[43] N. Rakotomalala, D. Salin, and P. Watzky, "Miscible displacement between two parallel plates: BGK lattice gas simulations," *Journal of Fluid Mechanics*, vol. 338, pp. 277–297, May 1997.

[44] C. Denniston, E. Orlandini, and J. M. Yeomans, "Lattice Boltzmann simulations of liquid crystal hydrodynamics," *Physical Review E*, vol. 6305, pp. –, May 2001.

[45] A. Dupuis, A. J. Briant, C. M. Pooley, and J. M. Yeomans, "Droplet spreading on heterogeneous surfaces using a three-dimensional, lattice Boltzmann model," *Computational Science - ICCS 2003, Pt I, Proceedings*, vol. 2657, pp. 1024–1033, 2003.

[46] P. J. Dellar, "Lattice kinetic schemes for magnetohydrodynamics," *Journal of Computational Physics*, vol. 179, pp. 95–126, Jun. 2002.

[47] P. J. Dellar, "Lattice kinetic formulation for ferrofluids," *Journal of Statistical Physics*, vol. 121, pp. 105–118, Oct. 2005.

[48] D. O. Martinez, W. H. Matthaeus, S. Chen, and D. C. Montgomery, "Comparison of spectral method and lattice Boltzmann simulations of 2-dimensional hydrodynamics," *Physics of Fluids*, vol. 6, pp. 1285–1298, Mar. 1994.

[49] H. D. Yu, S. S. Girimaji, and L. S. Luo, "DNS and LES of decaying isotropic turbulence with and without frame rotation using lattice Boltzmann method," *Journal of Computational Physics*, vol. 209, pp. 599–616, Nov. 2005.

[50] B. Chopard and S. Marconi, "Lattice Boltzmann solid particles in a lattice Boltzmann fluid," *Journal of Statistical Physics*, vol. 107, pp. 23–37, Apr. 2002.

[51] S. Marconi and B. Chopard, "A lattice Boltzmann model for a solid body," *International Journal of Modern Physics B*, vol. 17, pp. 153–156, Jan. 2003.

[52] T. G. Goktekin, A. W. Bargteil, and J. F. O'Brien, "Method for animating viscoelastic fluids," *ACM Transactions on Graphics*, vol. 23, pp. 463–468, Aug. 2004.

[53] X. M. Wei, Y. Zhao, Z. Fan, W. Li, F. Qiu, S. Yoakum-Stover, and A. E. Kaufman, "Lattice-based flow field modeling," *IEEE Transactions on Visualization and Computer Graphics*, vol. 10, pp. 719–729, Nov.–Dec. 2004.

[54] J. Chin, E. S. Boek, and P. V. Coveney, "Lattice Boltzmann simulation of the flow of binary immiscible fluids with different viscosities using the Shan-Chen microscopic interaction model," *Philosophical Transactions of the Royal Society of London Series A–Mathematical Physical and Engineering Sciences*, vol. 360, pp. 547–558, Mar. 2002.

[55] J. Bernsdorf, S. E. Harrison, S. M. Smith, P. V. Lawford, and D. R. Hose, "Numerical simulation of clotting processes: a lattice Boltzmann application in medical physics," *Mathematics and Computers in Simulation*, vol. 72, pp. 89–92, Sep. 2006.

[56] E. Aharonov and D. H. Rothman, "Non-Newtonian flow (through porous-media) – a lattice-Boltzmann method," *Geophysical Research Letters*, vol. 20, pp. 679–682, Apr. 1993.

[57] I. Ginzburg and K. Steiner, "A free-surface lattice Boltzmann method for modelling the filling of expanding cavities by Bingham fluids," *Philosophical Transactions of the Royal Society of London Series A–Mathematical Physical and Engineering Sciences*, vol. 360, pp. 453–466, Mar. 2002.

[58] S. Gabbanelli, G. Drazer, and J. Koplik, "Lattice Boltzmann method for non-Newtonian (power-law) fluids," *Physical Review E*, vol. 72, pp. –, Oct 2005.

[59] W. T. Kim, H. G. Chen, and M. S. Jhon, "Viscoelastic liquid bearing modeling via lattice Boltzmann method," *Journal of Applied Physics*, vol. 99, pp. –, Apr. 2006.

[60] I. Ispolatov and M. Grant, "Lattice Boltzmann method for viscoelastic fluids," *Physical Review E*, vol. 65, pp. –, May 2002.

[61] P. Lallemand, D. d'Humieres, L. S. Luo, and R. Rubinstein, "Theory of the lattice Boltzmann method: three-dimensional model for linear viscoelastic fluids," *Physical Review E*, vol. 67, pp. –, Feb. 2003.

[62] G. Giupponi and R. Coveney, "Non-Newtonian behaviour of the gyroid mesophase: a lattice-Boltzmann study," *Mathematics and Computers in Simulation*, vol. 72, pp. 124–127, Sep. 2006.

[63] P. Ahlrichs and B. Dunweg, "Simulation of a single polymer chain in solution by combining lattice Boltzmann and molecular dynamics," *Journal of Chemical Physics*, vol. 111, pp. 8225–8239, Nov. 1999.

[64] C. Cercignani, *The Boltzmann equation and its applications*. New York, NY: Springer-Verlag, 1988.

[65] H. Yu, "Lattice Boltzmann equation simulations of turbulence, mixing, and combustion," Ph.D. dissertation, Texas A&M University, College Station, Texas, 2006.

[66] X. Y. He and L. S. Luo, "*A priori* derivation of the lattice Boltzmann equation," *Physical Review E*, vol. 55, pp. R6333–R6336, Jun. 1997.

[67] D. Z. Yu, R. W. Mei, L. S. Luo, and S. Wei, "Viscous flow computations with the method of lattice Boltzmann equation," *Progress in Aerospace Sciences*, vol. 39, pp. 329–367, Jul. 2003.

[68] S. Y. Chen, D. Martinez, and R. W. Mei, "On boundary conditions in lattice Boltzmann methods," *Physics of Fluids*, vol. 8, pp. 2527–2536, Sep. 1996.

[69] J. S. Chong and D. M. Vezzi, "Unsteady flow of viscoelastic fluids," *Journal of Applied Polymer Science*, vol. 14, pp. 17–34, 1970.

APPENDIX A

DERIVATION FOR ADDITIONAL TERM IN THE EQUILIBRIUM DISTRIBUTION FUNCTION

In this appendix, we derive the additional term in the equilibrium distribution function due to the extra viscoelastic stress tensor. Now, momentum equation for a viscous fluid without any external forcing i.e., if Cauchy stress tensor $\sigma = -p\mathbf{I} + 2\mu\mathbf{D}$

$$\rho\left[\frac{\partial \mathbf{u}}{\partial t} + (\nabla \mathbf{u})\mathbf{u}\right] + div(p\mathbf{I}) = \mu\triangle\mathbf{u} \tag{A.1}$$

where $\triangle$ is the Laplace operator. The equilibrium distribution equation for this case is

$$f_i^{eq} = w_i\rho\left(1 + \frac{1}{3}\mathbf{e}\cdot\mathbf{u} + \frac{9}{2}(\mathbf{e}\cdot\mathbf{u})^2 - \frac{3}{2}\mathbf{u}\cdot\mathbf{u}\right) \tag{A.2}$$

When the Cauchy stress tensor $\sigma = -p\mathbf{I} + 2\mu\mathbf{D} + \triangle\sigma$, the momentum equation can be written as

$$\rho\left[\frac{\partial \mathbf{u}}{\partial t} + (\nabla \mathbf{u})\mathbf{u}\right] + div(p\mathbf{I} - \triangle\sigma) = \mu\triangle\mathbf{u} \tag{A.3}$$

Dellar [47] in his paper showed that, due to the additional stress tensor $\triangle\sigma$, the equilibrium distribution function would be

$$\begin{aligned} f_i^{eq} = {} & w_i\rho\left(1 + \frac{1}{3}\mathbf{e}\cdot\mathbf{u} + \frac{9}{2}(\mathbf{e}\cdot\mathbf{u})^2 - \frac{3}{2}\mathbf{u}\cdot\mathbf{u}\right) \\ & - \frac{9w_i}{2}(\mathbf{e}_i\mathbf{e}_i - \frac{1}{3}\mathbf{I}) : (-\triangle\sigma - \frac{1}{3}(Tr(-\triangle\sigma))) \end{aligned} \tag{A.4}$$

Now,

$$\begin{aligned} (\mathbf{S} - \frac{1}{3}\mathbf{I}(tr\mathbf{S}))_{ij} &= \mathbf{S}_{ij} - \frac{1}{3}(tr\mathbf{S})\delta_{ij} \\ \text{and} \quad (\mathbf{ee} - \frac{1}{3}\mathbf{I})_{ij} &= \mathbf{e}_i\mathbf{e}_j - \frac{1}{3}\delta_{ij} \end{aligned} \tag{A.5}$$

So,

$$\begin{aligned}\mathbf{ee} - \frac{1}{3}\mathbf{I} : (\mathbf{S} - \frac{1}{3}\mathbf{I}(tr\mathbf{S})) &= \mathbf{e}_i\mathbf{e}_j\mathbf{S}_{ji} - \frac{1}{3}(tr\mathbf{S}) - \frac{1}{3}(tr\mathbf{S})|\mathbf{e}|^2 + \frac{1}{9}(tr\mathbf{S})(tr\mathbf{I}) \\ &= \mathbf{e}_i\mathbf{e}_j\mathbf{S}_{ji} + \frac{1}{3}(tr\mathbf{S})[\frac{1}{3}(tr\mathbf{I}) - |\mathbf{e}|^2 - 1]\end{aligned} \tag{A.6}$$

If D is the number of dimensions, then $tr\mathbf{I} = D$ equation (A.6) becomes

$$(\mathbf{ee} - \frac{1}{3}\mathbf{I}) : (\mathbf{S} - \frac{1}{3}\mathbf{I}(tr\mathbf{S})) = \mathbf{e}_i\mathbf{e}_j\mathbf{S}_{ji} + \frac{1}{3}(tr\mathbf{S})[\frac{1}{3}D - |\mathbf{e}|^2 - 1] \tag{A.7}$$

Let us look at the case when $S = -\triangle\sigma = -\mathbf{T}$

$$\begin{aligned}(\mathbf{ee} - \frac{1}{3}\mathbf{I}) : (\mathbf{S} - \frac{1}{3}\mathbf{I}(tr\mathbf{S})) &= \mathbf{e}_i\mathbf{e}_j\left[-\mathbf{T}_{ji}\right] \\ &\quad + \frac{1}{3}\left[-\mathbf{T}_{ii}\right]\left[\frac{1}{3}D - |\mathbf{e}|^2 - 1\right]\end{aligned} \tag{A.8}$$

Hence,

$$(\mathbf{e}_\alpha\mathbf{e}_\alpha - \frac{1}{3}\mathbf{I}) : (\mathbf{S} - \frac{1}{3}\mathbf{I}(tr\mathbf{S})) = -\mathbf{e}_{\alpha i}\mathbf{e}_{\alpha j}\mathbf{T}_{ji} - \frac{1}{3}\left[\frac{D}{3} - 1 - |\mathbf{e}_\alpha|^2\right]\mathbf{T}_{ii} \tag{A.9}$$

And so, the new equilibrium distribution equation would be

$$\begin{aligned}f_\alpha^{eq} &= w_\alpha\rho\left(1 + \frac{1}{3}\mathbf{e}_\alpha\cdot\mathbf{u} + \frac{9}{2}(\mathbf{e}_\alpha\cdot\mathbf{u})^2 - \frac{3}{2}\mathbf{u}\cdot\mathbf{u}\right) \\ &\quad - \frac{9}{2}w_\alpha\mathbf{e}_{\alpha i}\mathbf{e}_{\alpha j}\mathbf{T}_{ji} - \frac{3}{2}w_\alpha\left(\frac{D}{3} - 1 - |\mathbf{e}_\alpha|^2\right)\mathbf{T}_{ii}\end{aligned} \tag{A.10}$$

VITA

Satish Karra

Department of Mechanical Engineering, Texas A&M University,

College Station, TX – 77840

EDUCATION

May '07: *M.S* Mechanical Engineering, Texas A&M University, College Station, TX.

May '05: *B.Tech* Mechanical Engineering, Indian Institute of Technology Madras, India.

EXPERIENCE

Spring '07: *Graduate Assistant Teaching*, Texas A&M University, College Station, TX.

Fall '06: *Graduate Assistant Research*, Texas A&M University, College Station, TX.

Fall '05–Summer'06: *Graduate Assistant Teaching*, Texas A&M University, College Station, TX.